1996-09

Modeling of crack initiation and growth in solid rocket propellants using macromechanics and micromechanics theories

Lee, James H.

Monterey, California. Naval Postgraduate School

NAVAL POSTGRADUATE SCHOOL
MONTEREY, CALIFORNIA

THESIS

MODELING OF CRACK INITIATION AND GROWTH IN SOLID ROCKET PROPELLANTS USING MACROMECHANICS AND MICROMECHANICS THEORIES

by

James H. Lee

September 1996

Thesis Advisor: Young W. Kwon

Approved for public release; distribution is unlimited.

REPORT DOCUMENTATION PAGE

Form Approved OMB No. 0704-0188

1. AGENCY USE ONLY *(Leave blank)*	2. REPORT DATE September 1996.	3. REPORT TYPE AND DATES COVERED Master's Thesis

4. TITLE AND SUBTITLE SIMPLIFIED Modeling of Crack Initiation and Growth In Solid Rocket Propellants Using Macromechanics and Micromechanics Theories

5. FUNDING NUMBERS

6. AUTHOR(S) James H. Lee

7. PERFORMING ORGANIZATION NAME(S) AND ADDRESS(ES)
Naval Postgraduate School
Monterey CA 93943-5000

8. PERFORMING ORGANIZATION REPORT NUMBER

9. SPONSORING/MONITORING AGENCY NAME(S) AND ADDRESS(ES)

10. SPONSORING/MONITORING AGENCY REPORT NUMBER

11. SUPPLEMENTARY NOTES The views expressed in this thesis are those of the author and do not reflect the official policy or position of the Department of Defense or the U.S. Government.

12a. DISTRIBUTION/AVAILABILITY STATEMENT
Approved for public release; distribution is unlimited.

12b. DISTRIBUTION CODE

13. ABSTRACT *(maximum 200 words)*

Modeling and simulation of crack initiation and propagation in solid rocket propellant materials were conducted using both the macromechanics approach and the micro/macromechanics approach. Due to their composition, the solid rocket propellant can be construed as particle reinforced composites.

The macromechanics approach entailed a numerical simulation of a finite element model to predict the crack behavior based on the damage initiation, growth, and local saturation. Its results were then compared to the experimental data. In the simulation, it was assumed that a crack forms when a damage is saturated in a localized zone. The results from the simulation were quite comparable to the experimental results, validating the method of predicting crack initiation, growth, and arrest using the concept of damage growth and saturation.

The second approach involved using a simplified micromechanical model and the damage mechanics being applied at the micromechanics level and the finite element analysis being done subsequently at the macromechanics level. In using this approach, the damage modes such as matrix cracking, interface debonding and particle cracking were explainable in an explicit, fundamental manner. Several simulations were conducted using this approach including the cases of non-uniform particle distribution. The predicted results compared well with the experimental data.

14. SUBJECT TERMS Particulate Composites, Crack Initiation and Growth, Micromechanics, FEM, Damage Mechanics

15. NUMBER OF PAGES 97

16. PRICE CODE

17. SECURITY CLASSIFICATION OF REPORT	18. SECURITY CLASSIFICATION OF THIS PAGE	19. SECURITY CLASSIFICATION OF ABSTRACT	20. LIMITATION OF ABSTRACT
Unclassified	Unclassified	Unclassified	UL

NSN 7540-01-280-5500

Standard Form 298 (Rev. 2-89)
Prescribed by ANSI Std. 239-18 298-102

Approved for public release; distribution is unlimited.

MODELING OF CRACK INITIATION AND GROWTH IN SOLID ROCKET PROPELLANTS USING MACROMECHANICS AND MICROMECHANICS THEORIES

James H. Lee
Lieutenant, United States Navy
B.S., United States Naval Academy, 1990

Submitted in partial fulfillment
of the requirements for the degree of

MASTER OF SCIENCE IN MECHANICAL ENGINEERING

from the

NAVAL POSTGRADUATE SCHOOL
September 1996

Author: [redacted]
James H. Lee

Approved by: [redacted]
Young W. Kwon, Thesis Advisor

[redacted]
Terry R. McNelly, Chairman
Department of Mechanical Engineering

ABSTRACT

Modeling and simulation of crack initiation and propagation in solid rocket propellant materials were conducted using both the macromechanics approach and the micro/macromechanics approach. Due to their composition, the solid rocket propellant can be construed as particle reinforced composites.

The macromechanics approach entailed a numerical simulation of a finite element model to predict the crack behavior based on the damage initiation, growth, and local saturation. Its results were then compared to the experimental data. In the simulation, it was assumed that a crack forms when a damage is saturated in a localized zone. The results from the simulation were quite comparable to the experimental results, validating the method of predicting crack initiation, growth, and arrest using the concept of damage growth and saturation.

The second approach involved using a simplified micromechanical model and the damage mechanics being applied at the micromechanics level and the finite element analysis being done subsequently at the macromechanics level. In using this approach, the damage modes such as matrix cracking, interface debonding and particle cracking were explainable in an explicit, fundamental manner. Several simulations were conducted using this approach including the cases of non-uniform particle distribution. The predicted results comapred well with the experimental data.

TABLE OF CONTENTS

I. INTRODUCTION

Because of their light weight and stability, in the last few decades, solid propellants have replaced liquid fuel as the primary means of projecting rockets and missiles. Most missiles in use today such as the Tomahawk and the Harpoon employ solid propellants. Missiles like these, because of the nature of their use, require high level of accuracy and reliability. This means all systems onboard the missile are required to operate exactly to he designed specifications including the propulsion system. Solid propellants, despite their advantages, have few problem areas. One of these areas is the initiation of damage and cracks prior to and during operation. Microflaws over time tend to soften the mechanical behavior and increase the potential for the formation of a macroscopic crack. When this happens, the increased burning surface area as a result of the crack maybe enough to over-pressurize and thereby cause failure in the motor casing [Cornwell & Schapery (1975)]. Even if failure in the casing may not occur, the formation of the crack can cause uneven burning of the propellant leading to decrease in range of the missile.

The composition of solid propellants is such that it can be construed as a particle reinforced composite. More specifically, these composites are made up of a mixture of relatively soft, ductile matrix material, reinforced by randomly scattered, stiff particles. The advantages of these composites are increase in elastic modulus, increased strength, and/or increased toughness, all of which in varying degrees. [Ravichandran & Liu (1994)] The drawback

to these composites is that unlike the increase in stiffness or toughness, the benefit of the increase in strength is quite limited. [Johnson (1987)] As a result, it is critical to understand and to predict the failure mechanisms and the failure modes in the particle reinforced composites.

To understand the failure modes however, the strengthening factors must first be considered. Extensive studies by Bretchet (1990) revealed that the strength of the combined, composite material depends not only on the inherent material properties of the reinforcing particles but also on the size and the aspect ratio of these particles. They've concluded that the degree of influence of these factors depend on the Weibull modulus of the particles and the influence of these factors are greater in ductile materials as opposed to brittle materials. Similar study done by Shen (1993) in the effects of particle reinforcements to the effective elastic modulus of the composite material, showed that the cross-sectional shape and the spatial distribution of the reinforcing phase greatly influenced the elastic modulus. More specifically, it was found that in testing different shapes of reinforcing agents (of aspect ratio approximately equal to unity), the effective Young's modulus (at a fixed concentration of the phase) increased in the following order: double cone --> sphere --> Octagon --> unit cylinder. [Shen, Finot, Needleman, & Suresh (1993)] As for the distribution, it was found that an even distribution of the reinforcing agent throughout the composite material gave the greatest rise to the elastic modulus.

The objectives for this research were to develop a finite element model to accurately describe the experimental samples of particulate composites undergoing uniaxial loading and to develop simulation techniques to investigate damage, crack initiation, and growth in particulate composites. By providing an accurate method of predicting the crack initiation and propagation, the need for costly and time consuming experiments could be decreased. Also, parameters such as the loading condition and the material property can be changed easily for a computer simulation than for an actual experiment. Furthermore, these information help engineers and scientists understand the mechanisms of fracture in particle composites.

II. BACKGROUND LITERATURE REVIEW

In this study, two methods are used to model the crack initiation and growth. Although the specific procedure and the methods used in this study are unique, there have been similar studies done in the past that agree in principle and approach. In determining the effective properties of heterogeneous materials, Hashin (1962) utilizes variation theorems of the theory of elasticity to achieve upper and lower bounds for the Young's modulus. In his work, Hashin summarizes that in determining the elastic moduli of heterogeneous materials, they can be described by an elastic, isotropic matrix whose moduli are known. These isotropic particles are embedded with known homogenous elastic properties. Assuming also, that the volume fraction of the particles are evenly distributed and as a result, be regarded as quasi-homogenous and quasi-isotropic, the problem becomes finding the elastic moduli of this combined material. Specifically, his method derives the effective moduli involving only the stresses or strains inside the inclusions. This is done by considering the change in strain energy in a loaded homogenous body due to the inclusion of nonhomoeneities. He begins his derivation by applying the Hooke's law to the strain energy equation for an elastic, homogenous, isotropic material and then splitting the stress and strain tensors into isotropic and deviatoric parts, as shown in Equation (1).

$$U_0^{(\sigma)} = \frac{1}{2}\int_{(V)}\left(\frac{\sigma^{(0)^2}}{9K_m} + \frac{S_{ij}^{(0)}S_{ij}^{(0)}}{2G_m}\right)dV \qquad (1)$$

where

$$\sigma^{(0)} = \sigma_{kk}^{(0)},$$

$$s_{ij}^{(0)} = \sigma_{ij}^{0} - \frac{1}{3}\sigma^{(0)}\delta_{ij}$$

and K_m is the bulk modulus, G_m is the shear modulus, σ_{ij} is the stress tensor, and δ_{ij} is the Kronecker delta. Then, after including N particles into the material and applying surface tractions (tensile load in the vertical direction & compressive load in the horizontal direction), the strain energy stored in the composite body can be expressed by

$$U^{(\sigma)} = U_0 + \delta U^{(\sigma)} = U_0 + \sum_{n=1}^{n=N} \delta U_n^{(\sigma)} \qquad (2)$$

where

$$\delta U_n^{(\sigma)} = \frac{1}{2}\int_{(\overline{V}_n)} [(K_m - K_p)\varepsilon_{ij}^{(0)}\varepsilon_{ij} + 2(G_m - G_p)e_{ij}^{(0)}e_{ij}]dV \qquad (3)$$

where

$$\varepsilon_{ij}^{(0)} = \varepsilon_{kk}^{(0)}$$

$$e_{ij}^{(0)} = \varepsilon_{ij}^{(0)} - \tfrac{1}{3}\varepsilon^{(0)}\delta_{ij} \quad .$$

The notations with subscript of "0" refers to the same given body but with no inclusions and under the same load. ε_{ij} denotes the strain tensor, $\overline{V}_n$ denotes the volume of the nth inclusion, and the subscript "p" denotes the particle material and the corresponding stresses and strains are written without superscripts. By the above equations therefore, if the stresses and strains in the inclusions are known, then $U^{(\sigma)}$ can be determined. Now, assuming the

tractions loaded on the boundary surface is derived from a uniform stress system, $U^{(\sigma)}$ can then be expressed by Equation (2) where the stresses are constant and the moduli K_m and G_m can be replaced by the effective moduli K^* and G^*. Therefore,

$$U^{(\sigma)} = \frac{1}{2}\left(\frac{\sigma^{(0)^2}}{9K^*} + \frac{s_{ij}^{(0)} s_{ij}^{(0)}}{2G^*}\right)V \qquad (4)$$

where the explanation for various quantities are as previously given. Knowing $U^{(\sigma)}$ then, the above equation can then be expressed in terms of the effective moduli. [Hashin (1962)]

The damage modes of a particle reinforced composite are particle-matrix debonding called dewetting, matrix damage such as cavity formation, and particle cracking. If the difference in strength is significantly large between the matrix material and the reinforcing particles, the mode of damage or failure is usually dewetting or cavity formation in the matrix or both. Studies done by Schapery(1987), Anderson and Farris (1988), and Ravichandran and Liu (1995) have shown that these damages cause volume dilatation resulting in a nonlinear stress-strain behavior. In other words, they investigated the nonlinear constitutive response of the damaged particulate composite with the change in volume dilatation as a weighing factor. Micromechanical models were considered to describe the nonlinear stress-strain behavior with damage evolution in particle reinforced composites. These studies also included the failure modes,

dewetting and matrix cracking. Graphic representation of these failure modes are included in Figure 1.

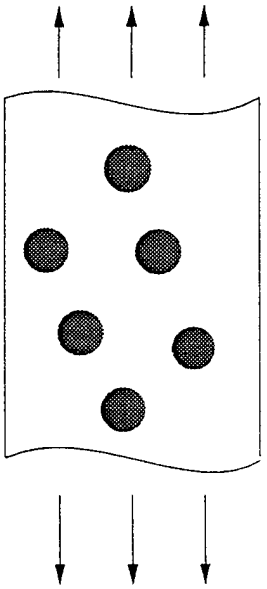

NO DEFECTS

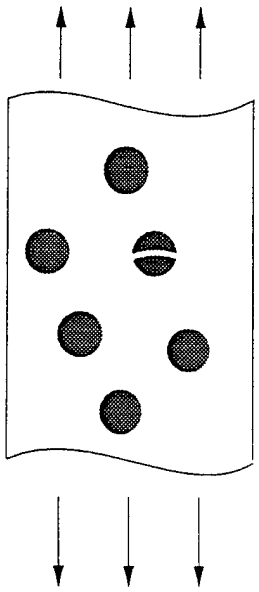

PARTICLE CRACKING

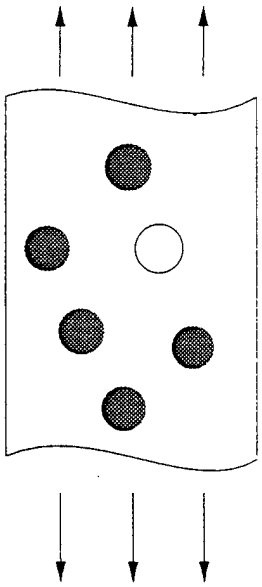

VOID INCLUSION

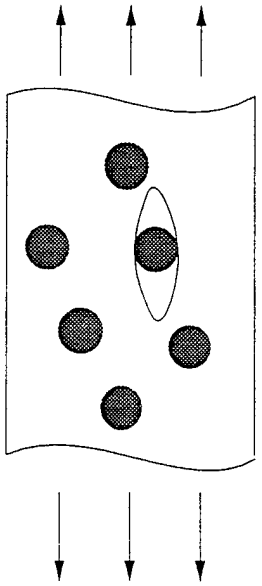

MATRIX-PARTICLE DEBONDING

Figure 1. Various Failure Modes

The application of micromechanics in predicting the effective properties and failure characteristics of composite materials is not unique to the present study. There in fact, exists several well-known models that have been developed, and Christensen brings these models together in a critical evaluation in regard to their range of applicability and their accuracy. The three micromechanics models which he considers are the Differential Method [Roscoe (1952)], the Generalized Self Consistent Method [Christensen and Lo (1979)], and the Mori-Tanaka Method [Benveniste (1987)]. His evaluation of the above methods is on a material with poly-dispersed spherical inclusions whose limiting case is specified by those orientations that allow complete packing with v.f. --> 1. There are several advantages for considering models that permit v.f. --> 1. First is that they are well suited for theoretical processing. As a result, they are widely used in theoretical studies. Second is that they model the actual, poly-disperse particle composites quite accurately, and the third is that they are an excellent approximations to the mono-disperse case for concentrations that are not too large. Christensen begins his evaluation with the Differential Method. The concept behind this method is to view the whole composite as a sequence of dilute suspensions and applying the below equations for the effective shear and bulk moduli (of an isotropic composite with non-interacting spherical inclusions) as each inclusion is added one at a time.

$$\frac{\mu}{\mu_m} = 1 + \frac{15(1-\nu_m)\left(\frac{\mu_i}{\mu_m} - 1\right)}{7 - 5\nu_m + 2(4-5\nu_m)\frac{\mu_i}{\mu_m}} c \tag{5}$$

and

$$\frac{k}{k_m} = 1 + \frac{\left(\frac{k_i}{k_m} - 1\right)}{1 + \left(\frac{k_i - k_m}{k_m + \frac{4}{3}\mu_m}\right)} c \tag{6}$$

where subscripts i and m denote inclusion and matrix, ν is the Poisson's ratio, μ and k denote effective shear and bulk modulus respectively, and c denotes the volume fraction of the particles. Therefore, after calculating μ and k with one inclusion, that suspension is considered as a homogenous material with those properties, to which the second inclusion is added, and the calculation is done again. The process continues until the condition of full packing of the inclusion is reached. The final result of this differential process is the set of governing equations:

$$\frac{d\mu}{dc} + \frac{15(1-\nu)(\mu - \mu_i)}{(1-c)\left[7 - 5\nu + 2(4-5\nu)\frac{\mu_i}{\mu}\right]} = 0 \tag{7}$$

and

$$\frac{dk}{dc} + \frac{(k - k_i)}{(1-c)\left[1 + \frac{k_i - k}{k + \frac{4}{3}\mu}\right]} = 0 \tag{8}$$

where effective Poisson's ratio ν is equal to

$$\nu = \frac{3k - 2\mu}{2(3k + \mu)} \tag{9}$$

The boundary conditions for the above equations are

$$\text{at } c = 0: \quad \mu = \mu_m \qquad k = k_m \tag{10}$$

$$\text{at } c = 1: \quad \mu = \mu_i \qquad k = k_i$$

The second method Christensen describes is the Generalized Self Consistent Method. The concept behind this method is to solve the equations derived from the model where a spherical inclusion is placed concentrically inside a matrix material which in turn are embedded in an effective medium with the properties of interest, μ and k. The model is mathematically represented by a quadratic equation,

$$A\left(\frac{\mu}{\mu_m}\right)^2 + 2B\left(\frac{\mu}{\mu_m}\right) + C = 0 \tag{11}$$

where the coefficients A, B, and C are equal to complex and rather tedious equations involving Poisson's ratio of the matrix and shear moduli of the inclusions and the matrix. The final result of the above quadratic equation is a closed form solution for the effective modulus,

$$k = k_m + \frac{c(k_i - k_m)}{1 + (1-c)\dfrac{(k_i \quad k_m)}{\left(k_m + \dfrac{4}{3}\mu_m\right)}} \qquad (12)$$

The final micromechanics analysis Christensen presents is the Mori-Tanaka Method. The Mori-Tanaka Method is significantly different from the first two models in that where as the first two methods concede physical descriptions, the Mori-Tanaka Method relies on mathematical manipulation of the field variables along with special concepts of eigenstrain and backstress. For the development of this method, Christensen cites Benveniste (1987) who developed a simplified derivation of the method. (However, even the simplified method is fairly extensive.) Since the derivation is quite involved, just the final result will be presented. The manipulation of Mori-Tanaka Method yields,

$$k = k_m + c(k_i - k_m)\frac{1}{1 + (1-c)\left[\dfrac{k_i - k_m}{k_m + \dfrac{4}{3}\dfrac{\mu_m}{k_m}}\right]} \qquad (13)$$

Having presented the details of the three micromechanics models, Christensen then evaluates the three methods in terms of their compatibility to the experimental results. The conclusion he makes based on the evaluation is that the Generalized Self Consistent Method is the most accurate of the three methods in determining the effective properties of the composite material, especially in the limiting case of a concentrated, poly-disperse suspension of rigid particles.

The other two models gave inaccurate and unrealistic behavior in the limiting case. [Christensen (1989)]

III. PRE-ANALYSIS PROCEDURE AND MODELING

A. PROCEDURE

Initially, a 2-D Finite Element Model was developed using the IDEAS program produced by SDRC. Once the models were generated, the mesh and nodal connectivity information was converted to an "ASCII" universal file and extracted from IDEAS. This information was read into a locally developed, general purpose FORTRAN finite element analysis program which could be set up in various ways to provide desired information such as effective stress, displacement, principle stress, micro-stresses etc. In executing this step, however, some modifications had to be made to the input data. Specifically, the universal output file from the IDEAS program had to be fitted into a format which the FORTRAN program could understand. This was done using a simple FORTRAN code which discarded unnecessary information from the universal file and place the remaining data in a suitable form. Some problems that were encountered during this process included: (1) the local nodal mapping which IDEAS used was in the direction opposite to the FORTRAN FEA program and (2) the rotation constraints had to be left at a value of "0" (i.e. no constraint) for the FEA program to work. Identifying and solving these compatibility problems between the IDEAS program and the FORTRAN FEA program posed significant obstacles in the progress of the research. Once the mesh information was successfully entered into the FORTRAN program, the rest of the input data such as the boundary conditions, applied loads, and material properties

were entered. The details of determining these input conditions is discussed in the next section.

B. FINITE ELEMENT MODELING

The driving condition for the FEM models in terms of their physical description was the experimental samples. The dimensions of the experimental samples, and hence, the FEM models, are shown in Figures 2 and 3. As can be seen, two samples were experimented. One was a 3 in. by 2.5 in. sample with a .5 in. diameter hole, and the other was a 3 in. by 2.5 in. sample with a .25 in. diameter hole. These samples were placed in an uniaxial loading machine and were loaded to .2 in/in strain. To model the experiment, a quarter section of the experimental samples was used, as can be seen in the figures. As for the finite element mesh, due to the constraints in the computer memory, there were limitations in number of nodes and elements that could be used. For both of the sample models, 750 elements and 806 nodes were used. As was found later during the computational phase however, the degree of freedom of the mesh was still too large for the computer to handle. Therefore, further manipulation of the mesh was necessary. In the IDEAS program, there exists several functions which sequentialize the nodes in a way that decreases the bandwidth of the global matrix used in the calculations. After several different variations of nodal sequencing, it was found that sweeping the mesh through y, then x-axis and subsequently applying the Sloan profile reduction scheme was optimum. By doing this, the bandwidth decreased from 58 to 27 which was within the capability of the computer. The

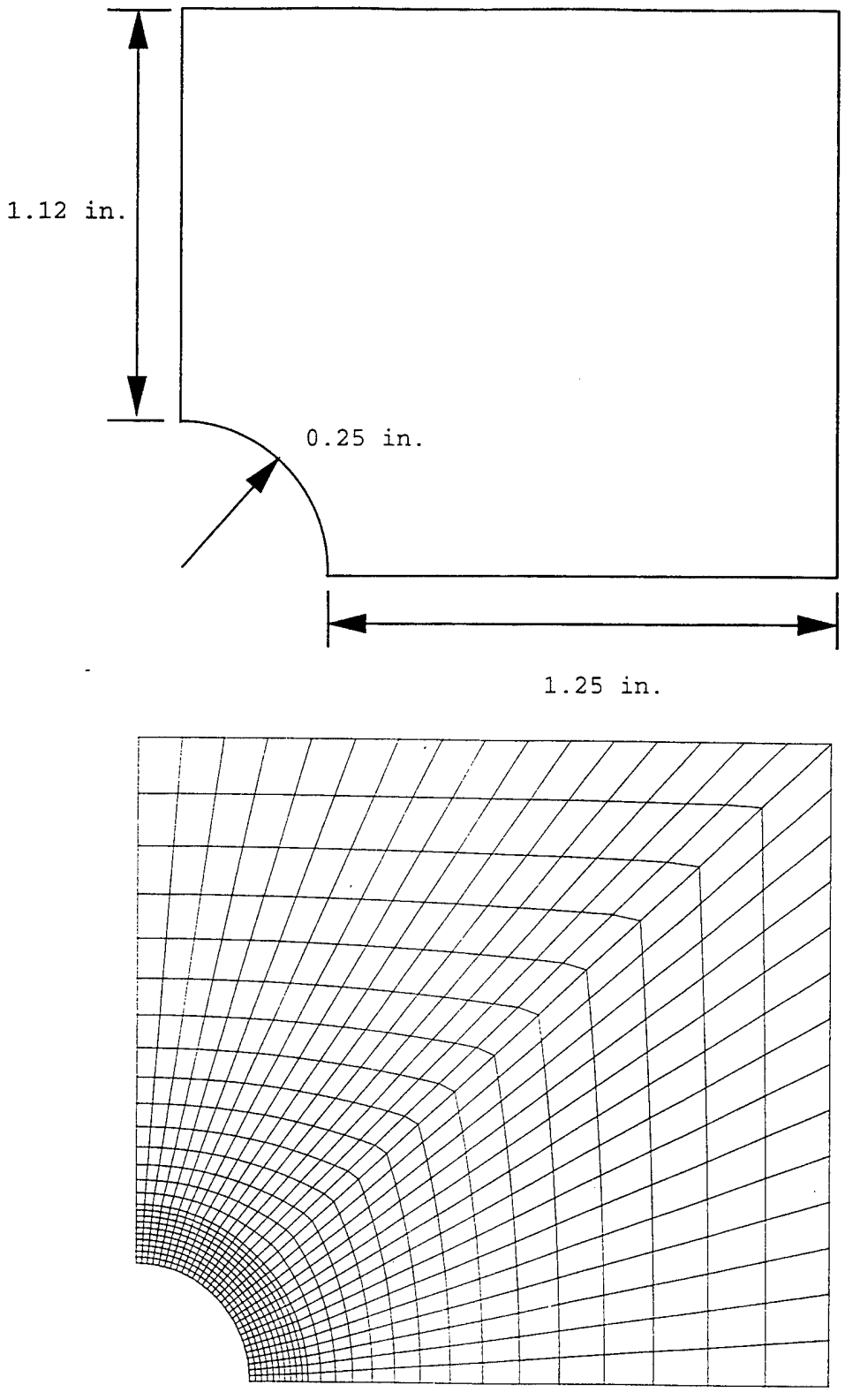

Figure 2. Finite Element Model of Larger Hole Sample

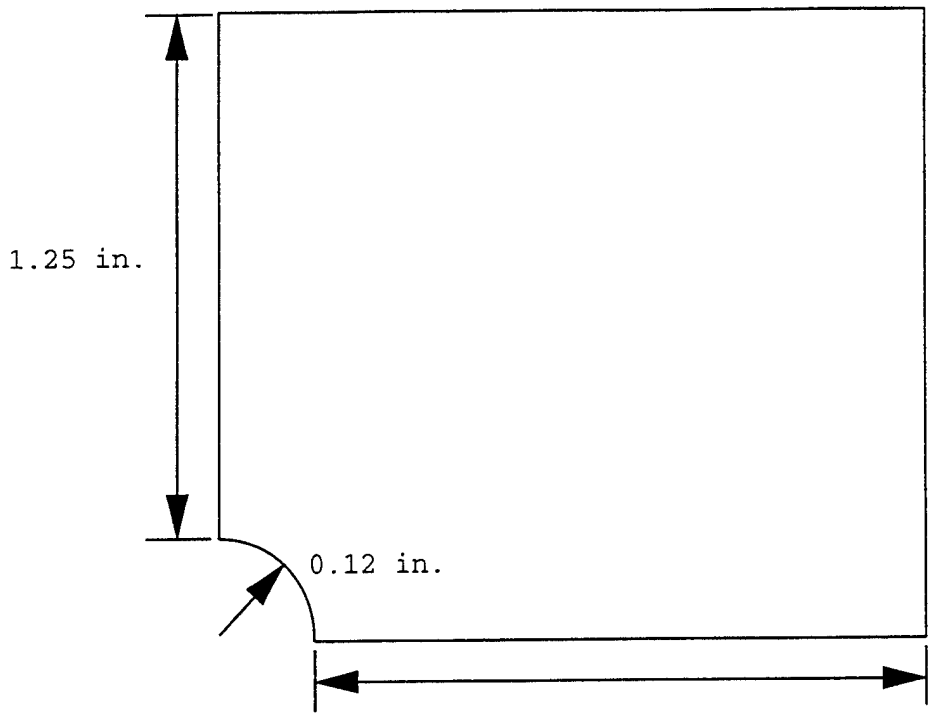

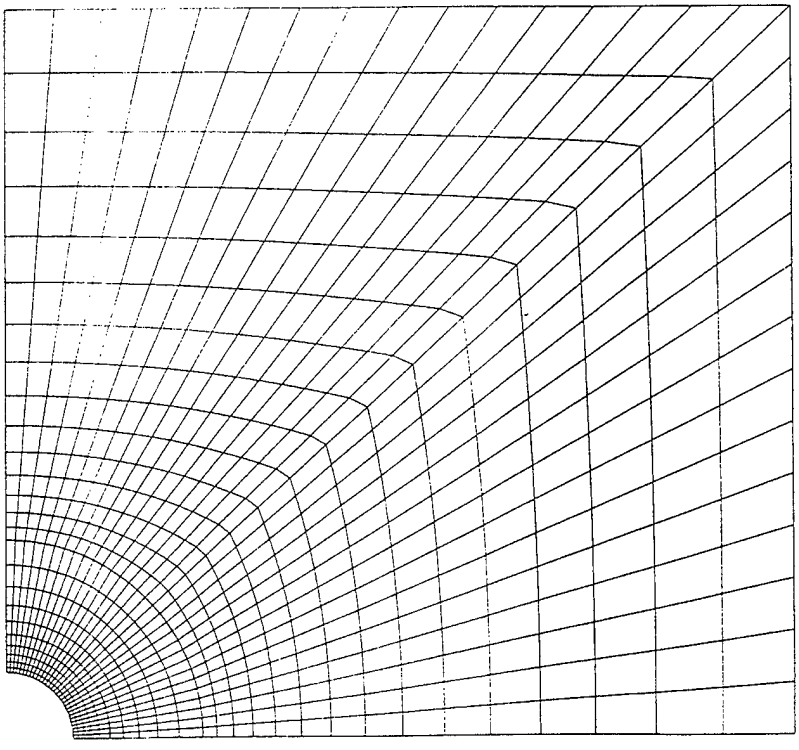

Figure 3. Finite Element Model of Smaller Hole Sample

next step in the modeling process was to apply proper constrains and boundary conditions. Since the FEM model represented a quarter section of the actual experimental sample, in order to accurately describe the experimental conditions, the left vertical edge was constrained in the x-direction, and the bottom horizontal edge was constrained in the y-direction, with the left corner point being constrained in both x and y-directions. The load was placed uniformly on the top vertical edge of the model. This is shown graphically in Figure 4. As for determining the behavior of the material, two conditions were considered, the geometric linear and the nonlinear. Initial studies indicated that the results from the nonlinear model was more realistic in terms of crack size for a given load and the shape of the damage zone near a stress concentration area.

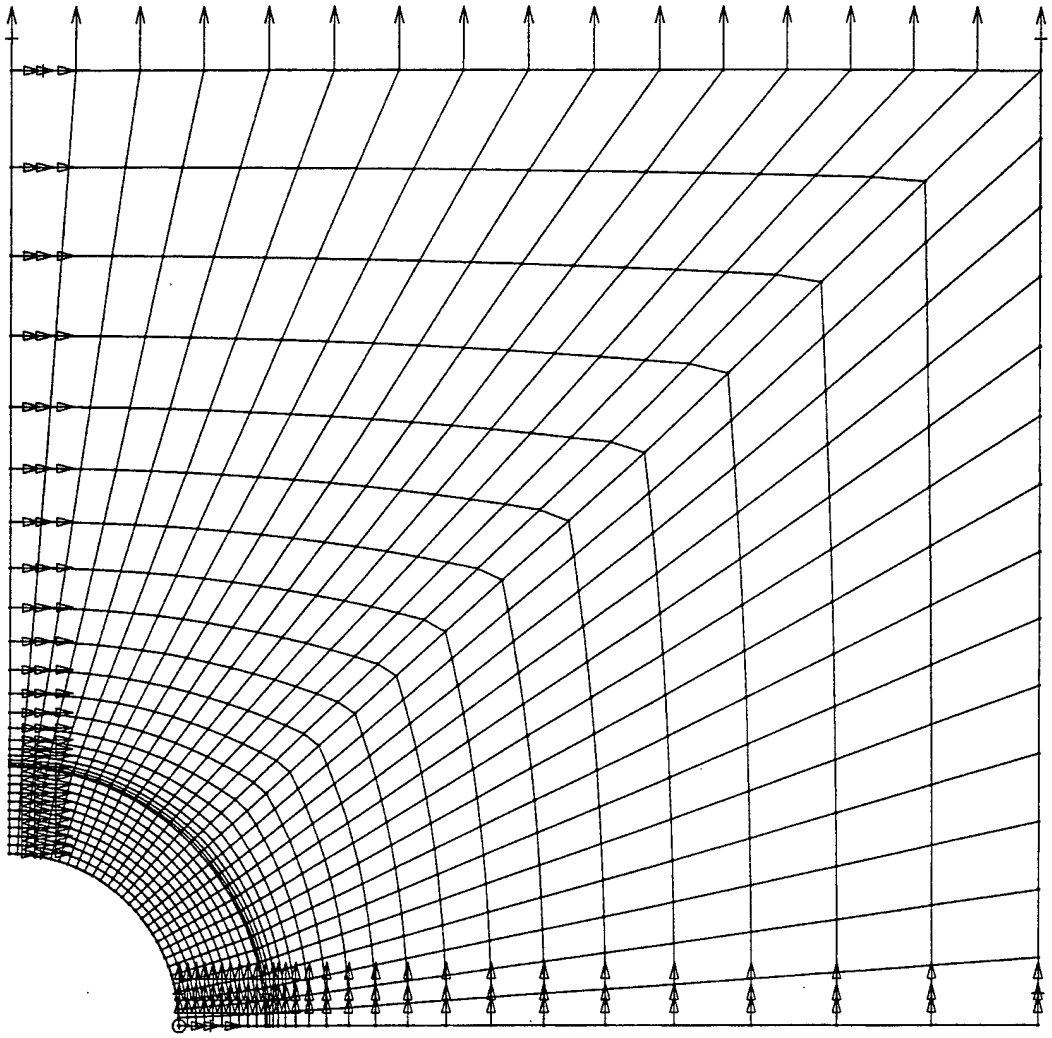

Figure 4. FE Model with Constraints and Loads Shown

IV. MACROMECHANICS MODELING AND ANALYSIS

A. MODELING AND APPROACH

In order to simulate the experiment conducted for the study of damage/crack initiation and propagation of a particle reinforced composite material, the finite element method was used. The FEM used in the study was dictated by the nonlinear elastic behavior of the composite material. Figure 5 shows a typical stress-strain plot of a particle reinforced composite material having undergone a uniaxial, tensile test. The figure also shows the volume dilatation of the material as a function of strain. The figure shows that the stress-strain curve begins linearly, and as the volume dilatation begins to increase, it starts to behave nonlinearly. After the continuous nonlinear behavior, the stress-strain curve reaches the peak point and the failure of the specimen occurs. The graph also shows the monotonic increase in volume dilatation until the peak point of stress value. This increase in volume dilatation results from the formation of cavities in the composite material during its continuous deformation. Therefore, the nonlinear behavior of the stress-strain curve can be attributed to these micro-damages in the material such as formation of cavities. In this regard therefore, the starting point on the stress-strain curve where nonlinearity begins to take effect is the point at which the damage or crack initiates. On the same token, the peak stress point on the curve represents the damage saturation state. These two points are marked in Figure 5.

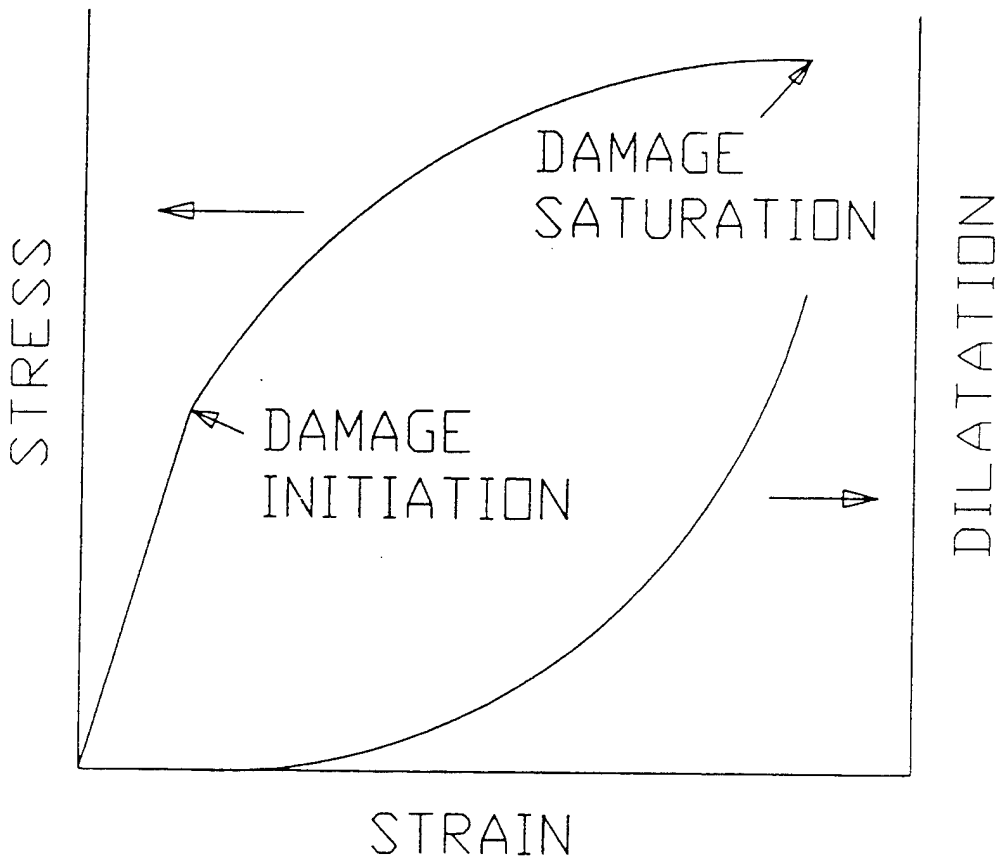

Figure 5. Stress-Strain and Dilatation Curves

The nonlinear stress-strain curve is used in the finite element analysis in order to model the damage initiation, growth, and saturation in the composite material. The curve was discretized into a piecewise linear curve which was then applied to the finite element analysis. The actual stress-strain curve used in the numerical analysis is shown in Figure 6. In extending the uniaxial stress information given by the stress-strain curve to the multiaxial state of stress, which is the case in the experiment, the von Mises equivalent stress is utilized as shown below.

$$\bar{\sigma} = \frac{1}{\sqrt{2}}[(\sigma_1 - \sigma_2)^2 + (\sigma_2 - \sigma_3)^2 + (\sigma_3 - \sigma_1)^2]^{\frac{1}{2}} \qquad (14)$$

When the equivalent stress reaches the peak stress value at a local area, the area is considered to have reached the damage saturation point. As a result, when this occurs, the damaged material cannot sustain any additional load. Therefore, majority of the load is transferred away from the damaged zone to the adjacent, undamaged or partially damaged zones.

B. ANALYSIS OF THE EXPERIMENTAL DATA

Figure 7 shows the X-ray images of the crack propagation in a particulate composite specimen under mode I condition, uniaxial, tensile load along the y-axis. In the image, the crack is represented by the black color where as the specimen in the undamaged areas is shown in color white. The dark cluster of circular spots indicate the damage zone. The lighter cluster inside the cluster which is most

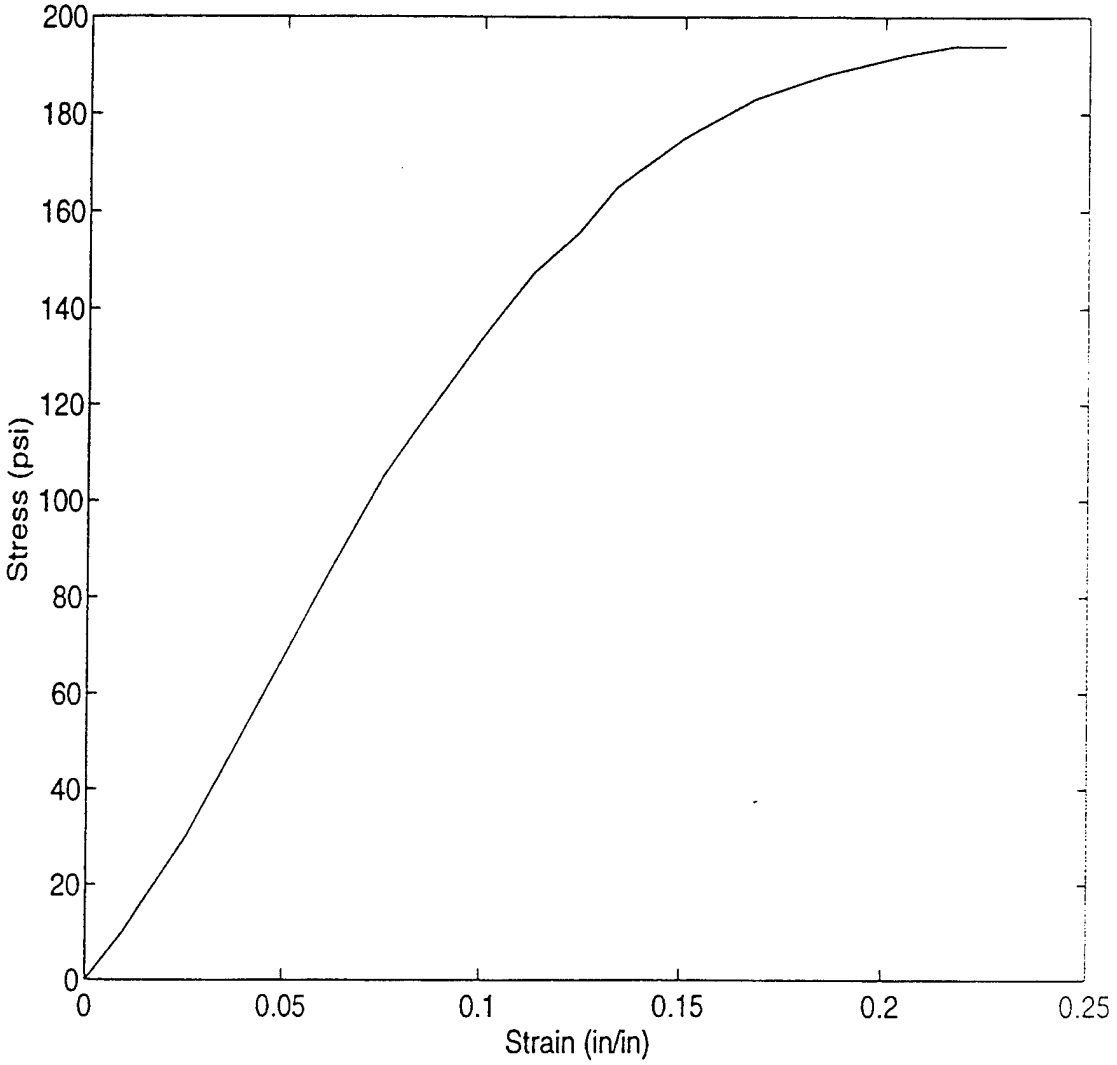

Figure 6. Uniaxial Stress-Strain Curve

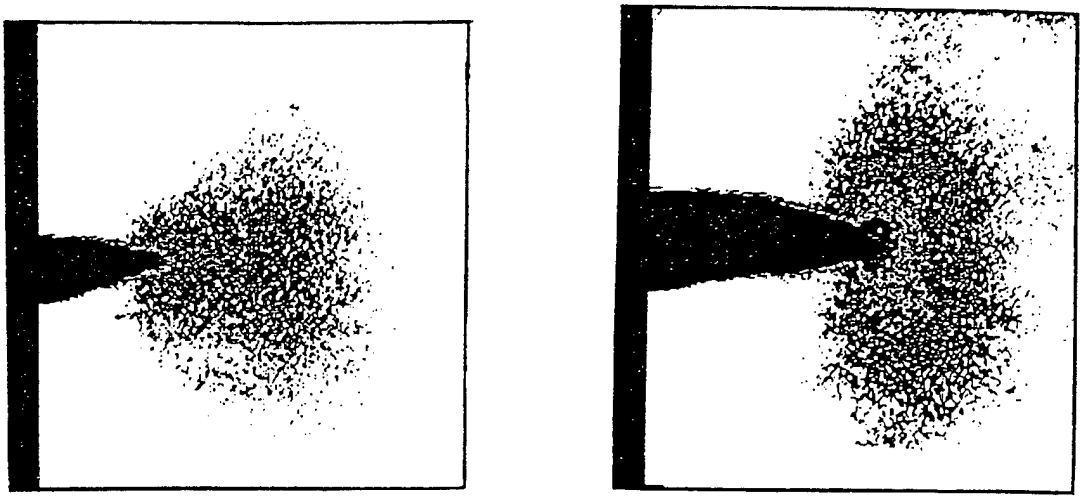

(a) (b)

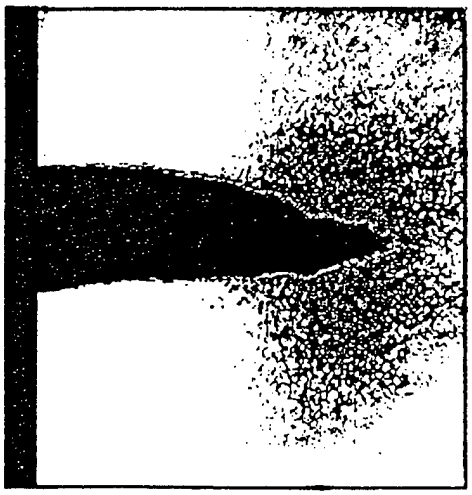

(c)

Figure 7. X-ray Pictures of Progressive Crack Propagation

clear in the second image represent a more damaged zone. As is visible in Figure 7(a), the damage zone develops and grows for the most part, in the direction of the crack. As the load increases, the damage zone grows and spreads in the vertical direction as seen in Figure 7(b). Notice the concentrated damage zone just ahead of the crack tip indicated by a lighter shade as the crack tip becomes blunt. Once the damage becomes saturated in front of the blunt crack tip, the crack propagates further protruding its tip as sharply as before prior to the blunting. Therefore, as it is seen clearly from the images, when the damage becomes saturated in a local region, the crack forms in the area. This again can be attributed to the coalescing of the micro-damages in the damage zone and forming a macro size crack. Hence, in the analysis of the FEM model, this reasoning was followed in determining the formation of the crack. In the analysis, the particle reinforced composite was assumed to behave elastically, In other words, the viscous effect was neglected, and the strain rate effect was not taken into account. Including these effects would be the logical next step in the follow on studies.

V. MICRO/MACROMECHANICS MODELING AND ANALYSIS

A. SUMMARY OF METHOD

The developed micro/macromechanical method utilizes a micro-level analysis in conjunction with a macro-level analysis, hence the name. The micro-level analysis includes computation of stresses and strains in the constituent materials, namely the reinforcing particulates and the binding matrix. The macro-level analysis involves structural analysis of the composite as a whole. As will be revealed, the two analyses were performed at different scales within the model but maintained interaction with one another. A graphical representation of the interaction between the two analyses is shown in Figure 8. The macromechanical analysis utilizes the finite element method for structural analysis of a composite in a way in which the composite structure can be analyzed generically. In other words, the analysis was conducted so that the solution can be in multiple forms depending on the information needed. In the micromechanical analysis, a simplified unit-cell model [Aboudi (1987,1989); Kwon (1993): Kwon and Berner (1994,1995)] is used. Also, on the unit-cell model, a damage mechanics [Kachanov (9172,1980); Krajcinovic (1983); Talreja (1985)] is applied. The simplified unit-cell model calculates stresses and strains at the constituent materials, and the damage mechanics is applied to the micromechanical model based on the found, micro-level stresses and strains. One advantage of this approach is that the damage modes and mechanisms can be described discriminately, in terms of the constituent materials. As a

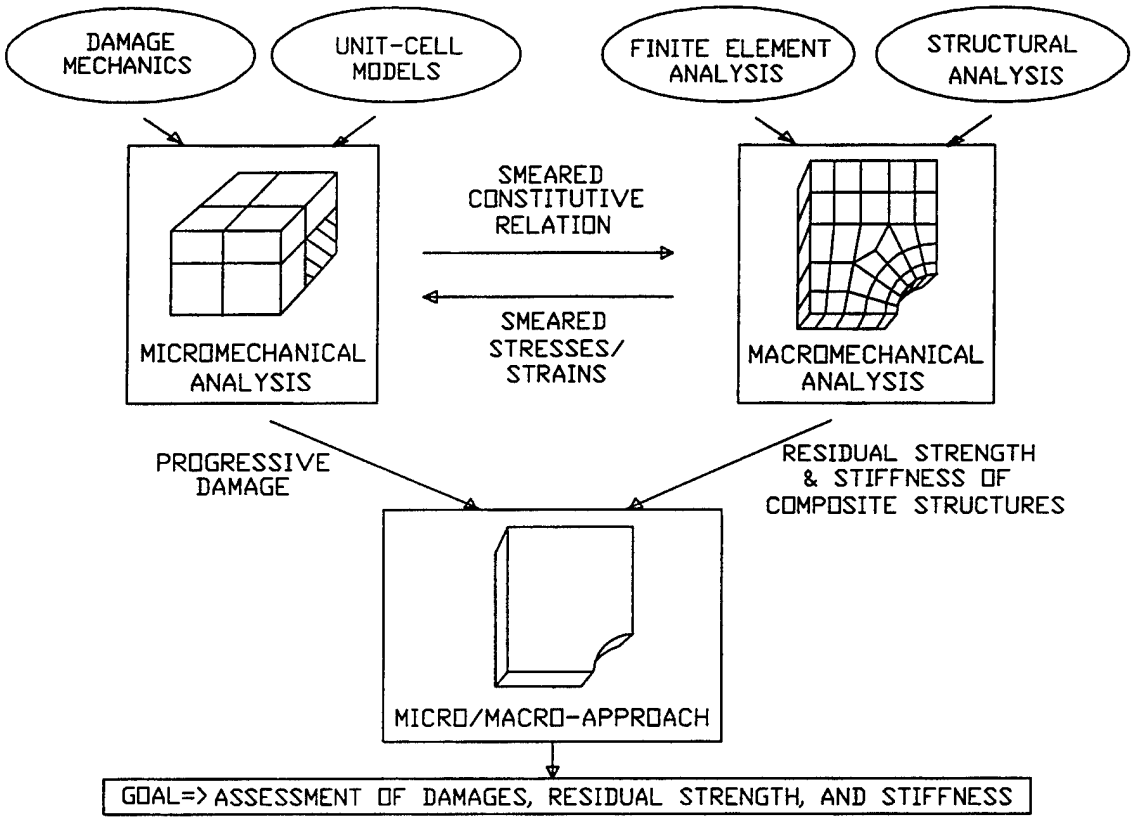

Figure 8. Relationship Between Micromechanics & Macromechanics

result, the damage modes can be specified as matrix cracking, particle cracking, or particle/matrix debonding. For the sake of emphasizing its exactness and the degree to which the analysis goes in depth, it is of interest to describe the interaction between the micromechanical and macromechanical analyses in detail. The micromechanical analysis computes the smeared composite material properties based on the constituent material properties and their damage states. This computation is conducted at every integration points of the macro-level, finite element model. Therefore, the finite element analysis can be undertaken as usual using the smeared composite material properties at the given integration points. After the macromechanical analysis is performed, the smeared stresses and strains at the composite level are then applied to the micromechanical model so that micro-level stresses and strains can be computed. This computation is performed at the same integration points as before. Therefore, as a result of fixing the points at which the numerical calculations are conducted, the interaction between the micro-level analysis and the macro-level analysis occurs at the integration points of the finite element model. And, the macromechanical model represents the material around each integration point. These domains around the integration points are dependent of the size of the finite element. Therefore, the damage state computed from the micromechanical analysis also indicates average damage of the area surrounding each integration point.

It should be apparent by now then, that by using the micromchanical approach, a particle reinforced composite with non-uniform distribution can easily be modeled.

B. UNIT-CELL MICROMECHANICAL MODEL

The micromechanical model is based on a unit cell structure. A unit cell consisting of a particle and the surrounding matrix material is modeled as shown in Figure 9. The figure shows a two-dimensional model. This is an adoption of the three-dimensional model which was studied by Kwon and Berner. (1994,1995) Due to symmetry, a quarter section of the full unit-cell model is considered, and that's what is shown in the figure. The quarter section of the unit-cell consists of four subcells of which the bottom left cell represents the particle inclusion and the rest of the surrounding three subcells represent the matrix material. By this model, it is assumed that the average deformation of the unit cell represents that of the particulate composite at each location.

The micromechanical model has two objectives: One is to compute the smeared composite material properties from particle and matrix material properties under an intact or a damaged state. The other is to describe damage modes and states at the specific, constituent material level. The development of the micromechanical model is described below. As stated before, this two-dimensional model is derived from the three-dimensional model which was developed previously. Each subcell has a constitutive equation expressed as

$$\sigma_{ij}{}^{\alpha} = E_{ijkl}{}^{\alpha}\varepsilon_{kl}{}^{\alpha} \qquad (15)$$

where i,j,k,l = 1,2 and α = a,b,c,d Here, 1 and 2 denote coordinate axes while a,b,c and d indicate subcells.

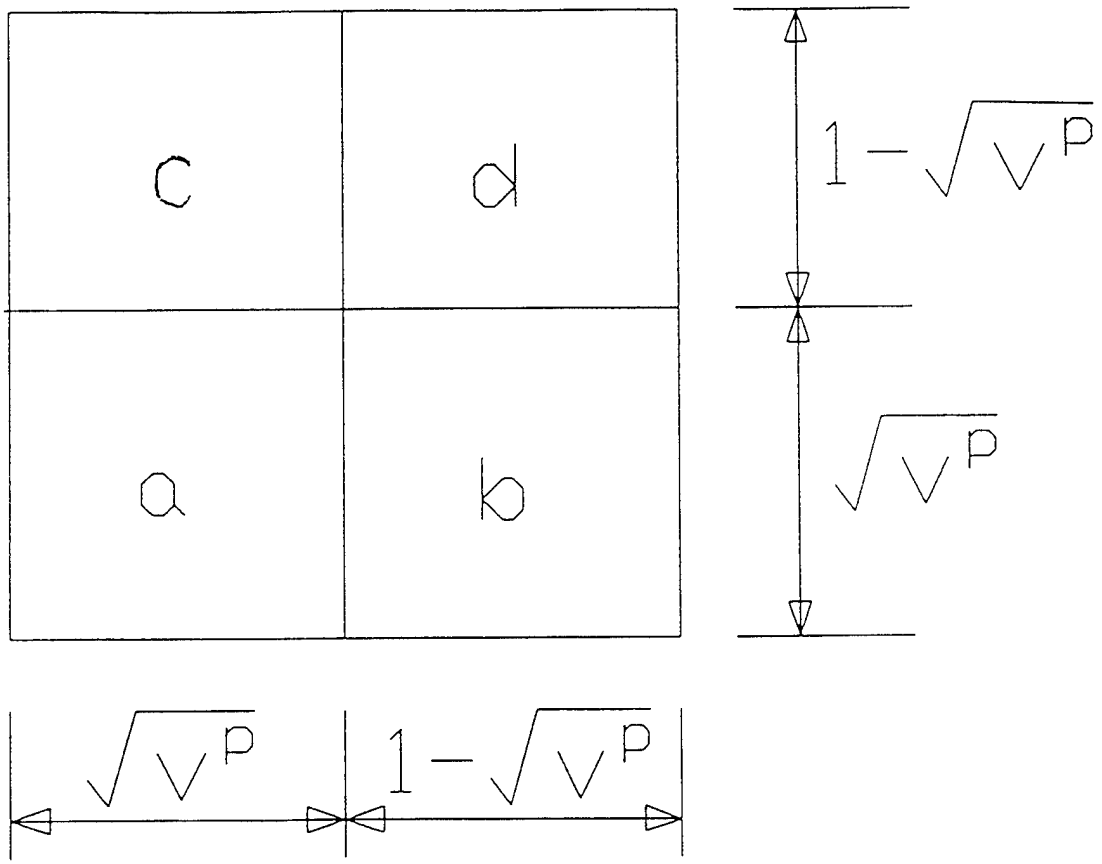

Figure 9. Simplified Unit-Cell Model

Subcell *a* represents the particle inclusion and the others represent the surrounding matrix material. σ_{ij}^{α} and $\varepsilon_{kl}^{\alpha}$ are the average stresses and strains of the subcell α. The unit cell stresses and strains are obtained from the volume average of the subcell stresses and strains. That is,

$$\bar{\sigma}_{ij} = V^a \sigma_{ij}^{\ a} + V^b \sigma_{ij}^{\ b} + V^c \sigma_{ij}^{\ c} + V^d \sigma_{ij}^{\ d} \tag{16}$$

$$\bar{\varepsilon}_{ij} = V^a \varepsilon_{ij}^{\ a} + V^b \varepsilon_{ij}^{\ b} + V^c \varepsilon_{ij}^{\ c} + V^d \varepsilon_{ij}^{\ d} \tag{17}$$

where $\bar{\sigma}_{ij}$ and $\bar{\varepsilon}_{ij}$ are the unit cell stresses and strains which eventually represent the smeared stresses and strains of the particulate composite. If there is no void present, the subcell volume fractions can be computed from the particle volume fraction bases on Figure 8.

$$V^a = V^p \tag{18}$$

$$V^b = V^c = \sqrt{V^p}(1-\sqrt{V^p})$$

$$V^d = (1-\sqrt{V^p})^2$$

in which V^p is the particle volume fraction.

One of the objectives of the micromechanical model is to find the relation between the unit cell stresses and strains (i.e. the constitutive relation at the composite level) using the material information at the subcell level. To this end, stress and strain compatibility equations are applied. First of all, the stress compatibility is considered at the subcell interfaces as given below.

$$\sigma_{11}^{a} = \sigma_{11}^{b} \tag{19}$$

$$\sigma_{11}^{c} = \sigma_{11}^{d}$$

$$\sigma_{22}^{a} = \sigma_{22}^{c}$$

$$\sigma_{22}^{b} = \sigma_{22}^{d}$$

$$\sigma_{12}^{a} = \sigma_{12}^{b} = \sigma_{12}^{c} = \sigma_{12}^{b}$$

Strain compatibility is assumed to be

$$\varepsilon_{11}^{a} + \varepsilon_{11}^{b} = \varepsilon_{11}^{c} + \varepsilon_{11}^{d} \tag{20}$$

$$\varepsilon_{22}^{a} + \varepsilon_{22}^{c} = \varepsilon_{22}^{b} + \varepsilon_{22}^{d}$$

Substitution of Equation (15) into the equations in (19) yields the stress compatibility equations in terms of subcell strains. Therefore, the equations in (19) become

$$E_{11kl}^{a}\varepsilon_{kl}^{a} = E_{11kl}^{b}\varepsilon_{kl}^{b} \tag{21}$$

$$E_{11kl}^{c}\varepsilon_{kl}^{c} = E_{11kl}^{d}\varepsilon_{kl}^{d}$$

$$E_{22kl}^{a}\varepsilon_{kl}^{a} = E_{22kl}^{c}\varepsilon_{kl}^{c}$$

$$E_{22kl}^{b}\varepsilon_{kl}^{b} = E_{22kl}^{d}\varepsilon_{kl}^{d}$$

$$E_{12kl}^{a}\varepsilon_{kl}^{a} = E_{12kl}^{b}\varepsilon_{kl}^{b} = E_{12kl}^{c}\varepsilon_{kl}^{c} = E_{12kl}^{d}\varepsilon_{kl}^{d}$$

These equations along with Equations (17) and (20) can relate the subcell strains to unit cell strains. That is,

$$[A]\{\varepsilon\} = \{\bar{\varepsilon}\} \tag{22}$$

in which $\{\varepsilon\}$ is a vector consisting of subcell strains $\varepsilon_{ij}^{\alpha}$ while $\{\bar{\varepsilon}\}$ is a vector consisting of the unit cell strains $\bar{\varepsilon}_{ij}$ and zeros. Solving Equation (22) results in the expression for the unit cell strains in terms of subcell strains. That is,

$$\{\varepsilon\} = [A]^{-1}\{\bar{\varepsilon}\} \tag{23}$$

Equation (23) gives the explicit relationship between the subcell and the unit cell strains (i.e. strains at the constituent level, the particle and the matrix, and strains at the composite level.) Equation (23) is very useful for damage and failure evaluation at the constituent level as will be discussed in the later chapter. Finally, in order to determine the constitutive relation between the unit cell stresses and strains, Equation (15) is substituted into Equation (16). This operation yields the expression for the unit cell stresses in terms of the subcell strains. The subcell strains are replaced by unit cell strains using Equation (23). AS a result, the unit cell stresses become directly related to the unit cell strains. The relating constitutive expression is given in terms of subcell material properties E_{ijlk}^{α} and subcell volume fractions V^{α}. In other words, the composite level constitutive equation is expressed in terms of the particle and matrix properties as given below.

$$\bar{\sigma}_{ij} = \bar{E}_{ijkl}\bar{\varepsilon}_{kl} \tag{24}$$

where $\bar{E}_{ijkl}$ is the constitutive relation of the composite.

C. DAMAGE MECHANICS

Application of the damage mechanics to the constituent materials, the matrix and the particle inclusions, is necessary in order to predict the damage initiation and evolution until the point of failure. By this application, the damage modes can be prescribed fundamentally and discriminately as matrix cracking, particle cracking or particle/matrix interface debonding. The present study considers matrix cracking with particle inclusions that are almost rigid.

For the development of the damage mechanics theory, the matrix material is considered. In the development, for the sake of simplicity, vector and matrix notations will be adopted instead of tensor notations. Therefore, stresses and strains are expressed in vector form, and the strain increment in the material may be written as,

$$\{d\varepsilon\} = \{d\varepsilon\}_v + \{d\varepsilon\}_d \tag{25}$$

where $\{d\varepsilon\}$ is the total strain increment, and the subscripts v and d denote the natural and damaged states, respectively. In short, the total strain increment consists of the strain increment without damage and the strain increment as a result of damage. The constitutive equation for the undamaged material is as follows:

$$\{d\sigma\} = [E]_v \{d\varepsilon\}_v \tag{26}$$

while the incremental strain due to the damage is assumed to be expressed as

$$\{d\varepsilon\}_d = d\lambda \frac{\partial F_d}{\partial \{\sigma\}} \tag{27}$$

in which F_d is the damage potential function. The damage potential function varies depending on the amount of damage state. Thus, it can be assumed that

$$F_d = F_d(\{\sigma\}, \{\varepsilon\}_d) \tag{28}$$

If the damage potential function is also used for the damage criteria, the damage state must satisfy $F_d = 0$. As a result, the Equation (28) can be written as

$$dF_d = \{\frac{\partial F_d}{\partial \{\sigma\}}\}^T \{d\sigma\} + \{\frac{\partial F_d}{\partial \{\varepsilon\}}\} \{d\varepsilon\} = 0 \tag{29}$$

Using Equations (25), (26) and (29), one can solve for $d\lambda$ as follows:

$$d\lambda = \frac{\{Q\}^T [E]_v \{d\varepsilon\}}{\{R\}^T \{Q\} + \{Q\}^T [E]_v \{Q\}} \tag{30}$$

where

$$\{Q\} = \{\frac{\partial F_d}{\partial \{\sigma\}}\} \tag{31}$$

and

$$\{R\} = \{\frac{\partial F_d}{\partial \{\varepsilon\}}\} \tag{32}$$

Substitution of Equation (30) into Equation (27) and combining the resultant equation with Equations (25) and (26) gives

$$\{d\sigma\} = [E]_d \{d\varepsilon\} \tag{33}$$

in which the constitutive matrix for the damaged material is

$$[E]_d = [E]_v ([I] - \frac{\{Q\}\{Q\}^T [E]_v}{\{R\}^T \{Q\} + \{Q\}^T [E]_v \{Q\}}) \tag{34}$$

The damage potential function is dependent on the constituent material and can be rewritten as

$$F_d = f(\{\sigma\}) - g((\varepsilon_d)_e) \tag{35}$$

in which f and g are assumed to be

$$f = (J_2')^{1/2} \tag{36}$$

and

$$g = \sigma_d + a_1 \tanh(a_2 (\varepsilon_d)_e) \tag{37}$$

Here, σ_d is the damage initiation strength of the material, $(\varepsilon_d)_e$ is the effective damage strain, and a_1 and a_2 are the

material constants. The material properties are determined from the uniaxial stress-strain curve, and the function g denotes the damage evolution.

VI. MACROMECHANICS RESULTS AND DISCUSSION

Damage initiation, growth, and saturation were observed from the analysis as the load increased. Again, Figure 6 shows the stress-strain curve of the material used in the study and the finite element mesh is shown in Figure 3. In order to simulate the experimental condition, a continuous, uniform strain was applied to the specimen in the modeling. In examining the circular hole, it was noted that the saturated damage zone at a lower value of the applied load was an elliptical shape with the major axis parallel to the load axis. Initially, the major diameter was much greater than the minor diameter. As the damage evolved, however, the minor diameter grew faster than the major diameter and the damage zone spread both in the load and crack directions. Figures 10, 11 and 12 shows this effect graphically. Figure 10 denotes the two regions in which the contour lines of the crack initiation and propagation are plotted. As can be seen from the figure, Region I denotes the area up to the eighth element in the x and y-directions which is 0.162 inches measured from the center of the hole. Region II denotes the area up to the twelfth element in the x and y-directions which is 0.308 inches from the center of the hole. Figure 11 is the magnified area of the Region I with section A denoting the area in which the crack has initiated. From the shape of section A, it seems as though the major axis of the crack is in the y-direction as opposed to in the x-direction which is contrary to the statement earlier. However, in looking at the initial crack area in relation to the area of the entire model, it is a very minute section. Therefore, Section A in Figure 11 is simply

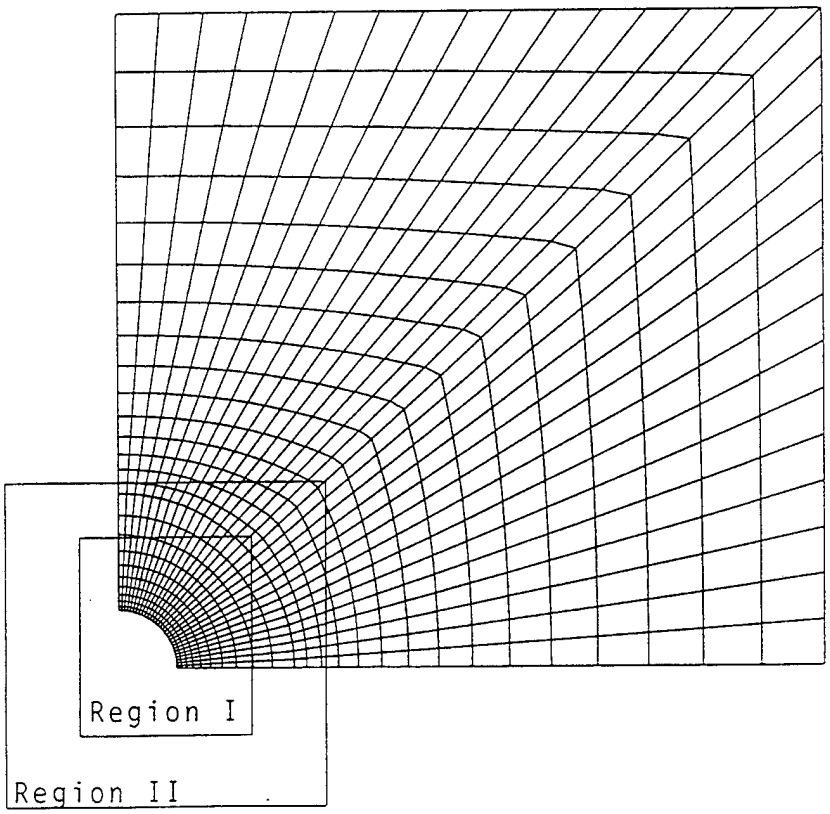

Figure 10. Regions Magnified in Figures 11 & 12

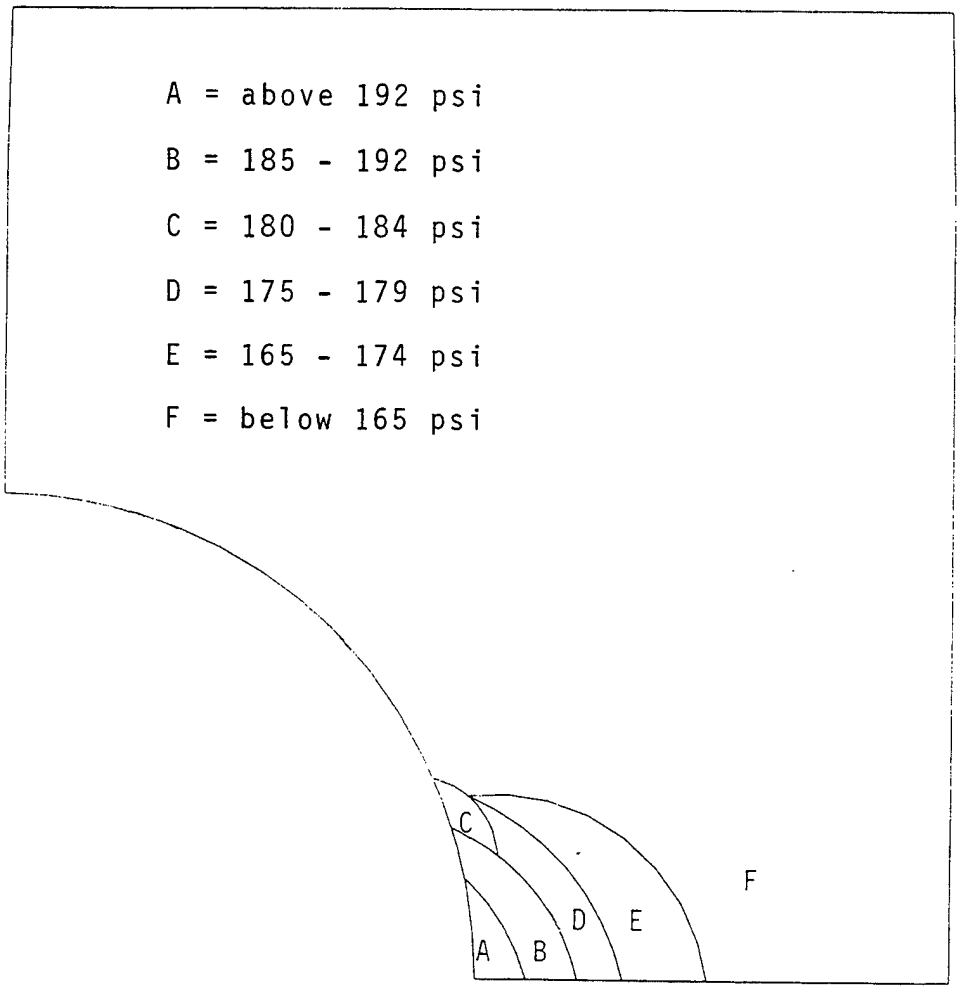

Figure 11. Magnified Region I with Contour Lines of Various Stress Levels

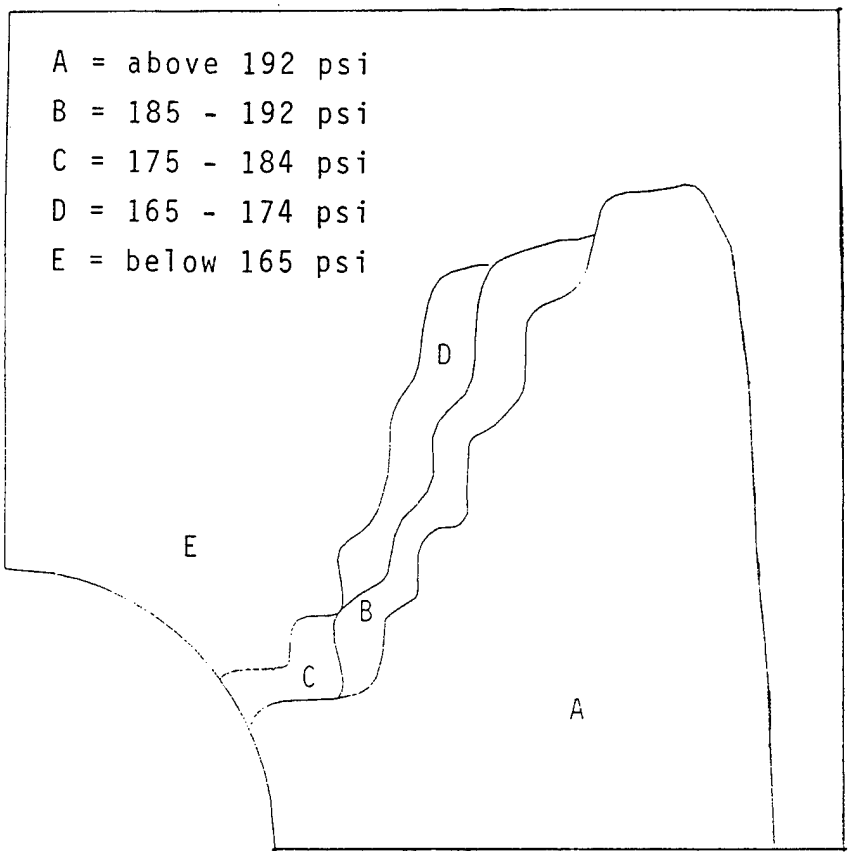

Figure 12. Magnified Region II with Contour Lines of Various Stress Levels

showing the location of the crack formation. It is not intended to show the shape of the crack propagation. To view the actual shape and the effect of the crack propagating in both vertical and horizontal direction, Figure 12 is provided. Figure 12 is the magnified area of Region II, and it shows section A whose area represent the propagation of the crack, and as can be seen, it is in both the horizontal and the vertical directions. From the information obtained through the numerical analysis concerning the final crack size at the load of .2 in/in strain, the experimental crack size was compared. As seen in Figure 13, the specimen compared well between the experimental and the numerical results. The experiment showed cracks of .795 cm (.313 in.) and .953 cm (.375 in.) at the two sides of the hole while the numerical simulation resulted in crack of .820 cm (.323 in.). The predicted crack was between the two experimental crack sizes. In the simulation, a quarter of the specimen was modeled as shown in Figure 3 due to symmetry. However, as shown by the slight difference in the crack sizes between the two sides, the actual specimen was not quite symmetric. There are many possible reasons for this asymmetry such as the location of the hole within the nonuniform material, the shape of the hole, and the nonunifrom surface roughness of the hole edge. A nonuniform particle distribution could be another factor causing such an asymmetry.

Figure 14 illustrates the simulated crack propagation as a function of the applied load for a specimen with an 1.27 cm (.5 in.) diameter hole. The simulation indicated

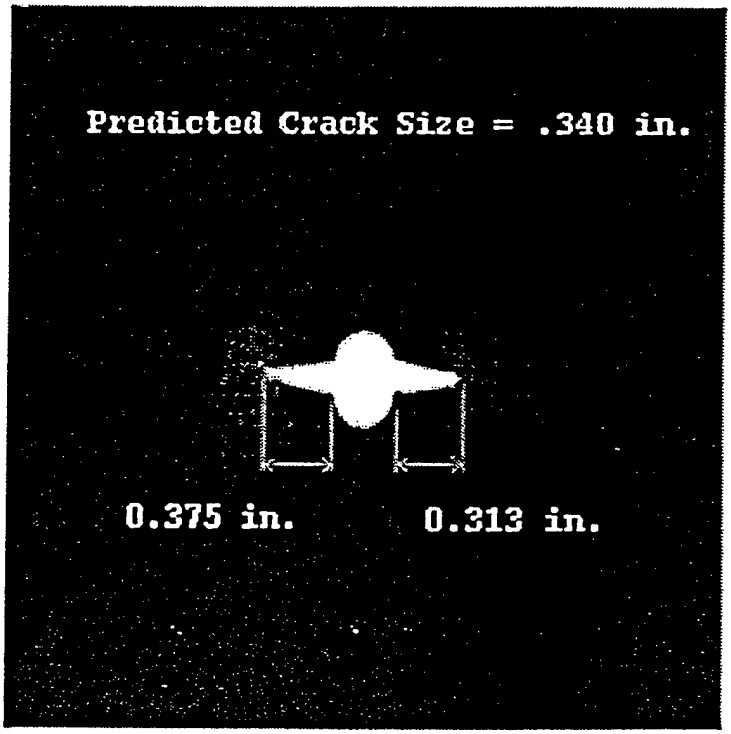

Figure 13. 0.25 in. Diameter Hole. Experimental with Predicted Results

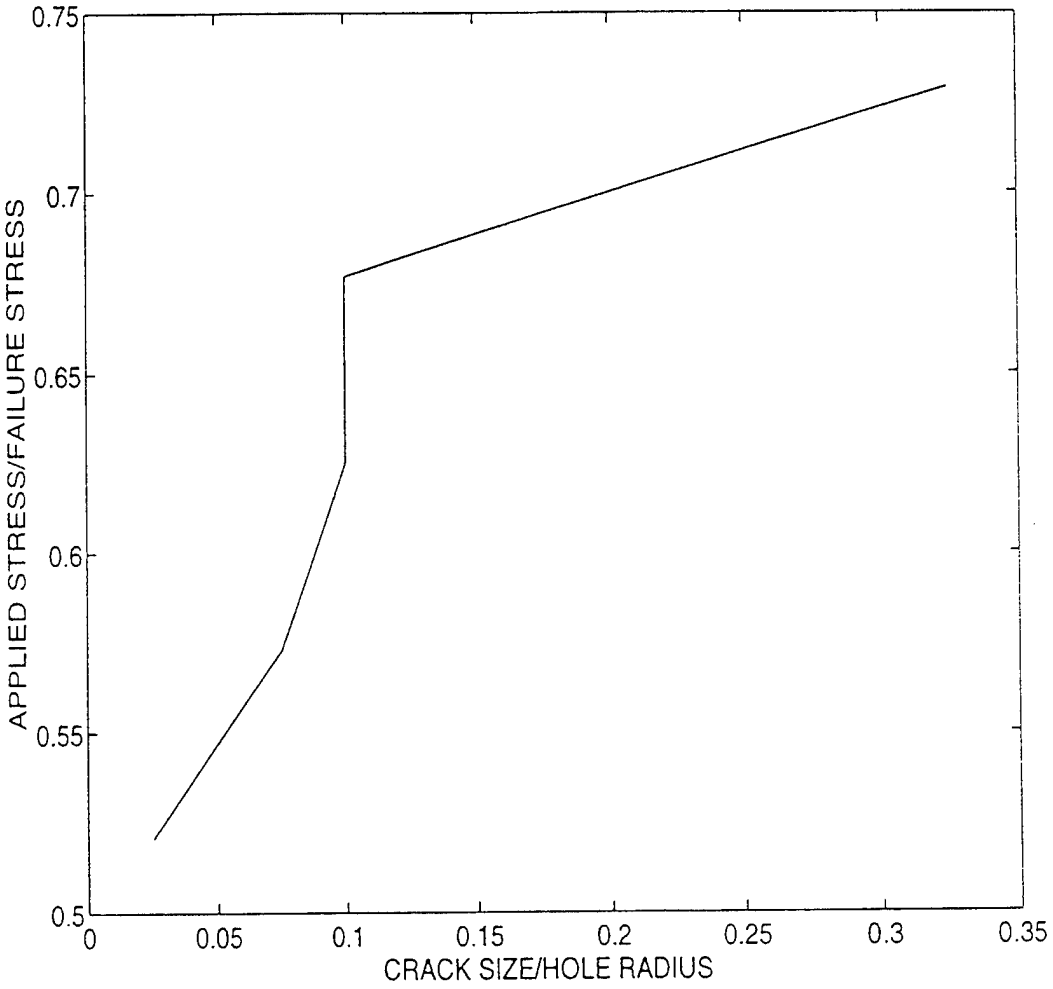

Figure 14. Simulated Crack Growth with Increasing Load for a Perforated Plate

that the resultant crack size increased with the increased applied load. Until the crack size became about 10 percent of the hole radius, which will be referred to as the critical crack size in the following discussions, the relationship between the applied load and the crack size was bilinear. At the critical cracks size, however, the increased loading propagated and accumulated the damage zone in the direction other than the crack orientation, mostly in the direction normal to the crack. Once there was a substantial increase in the load, the crack resumed propagation beyond the critical size in the direction of the crack orientation. Throughout the region, the crack propagation was linearly proportional to the applied load. The slope of the load verses the cracks size was less after the critical crack than the slope prior to the critical crack. The temporary halt of the crack propagation, shown as the vertical line segment in the graph, was an indication of the crack tip blunting process. As mentioned in the earlier section, this phenomena was also observed in the experimental study. (Refer to the second figure in Figure 5.) Recall how the damage zone concentrated around the crack tip causing the crack to become blunt as shown in the figure by a gray, circular patch of dots at the end of the crack tip.

Figure 15 is the tensile test coupon that was used to generate the stress-strain curve in Figure 6. The figure shows that the strain experienced is not uniform within the specimen. As shown, the specimen is divided into subsections A through E, positioned arbitrarily along the length of the coupon. The specimen was then stretched up to the strain value of .2 in/in. Figure 15 shows couple of

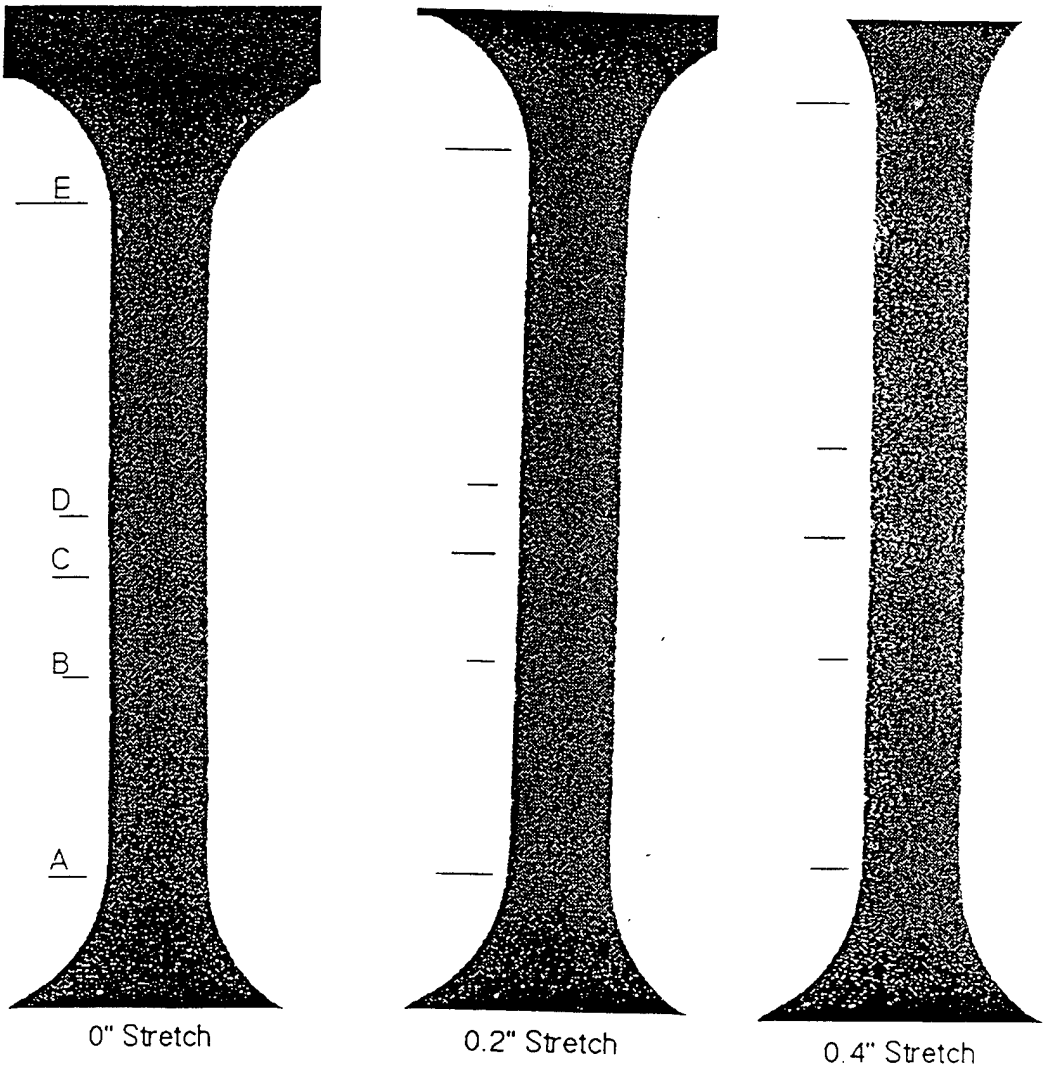

Figure 15. Deformation of a Tensile Specimen

representative pictures of how the specimen looked as the specimen under went loading. The next figure, Figure 16 shows the strain verses time at each of the subsections profiled against the strain of the whole length. As can be seen, the deformations at the various regions differed significantly. One of the major causes of the nonuniform deformations is the nonuniform particle distribution in the composite. The largest deformation occurs in the section CD where the curve is the steepest and the highest. The lowest position of the curve DE in the graph indicate the least amount of deformation. This can be interpreted as the region having most amount of particle inclusions. The overall deformation is indicated by the curve AE. As expected, the overall curve is nested between the subsection curves. Finally, all the curves in the graph follows a linear path in the deformation process except curve CD. Curve CD initially follows a path that has a slope similar to those of other curves until about two seconds into the deformation process. All of a sudden, the slope sharply increases indicating a greater amount of deformation per given time. As can be seen in Figure 11, section CD represents the small section in the middle of the sample. When the load is applied, this is the section where damage usually occurs. As a result, after a point in which the damage develops, the deformation of the material becomes more rapid and greater in magnitude.

Clearly, due to the behavior observed in the sample material, a nonuniform property should be assumed in the modeling. Therefore, for the specimen with a .635 cm (.25 in.) diameter hole, this was the case. In the next phase of the study, it was hypothesized that although the overall

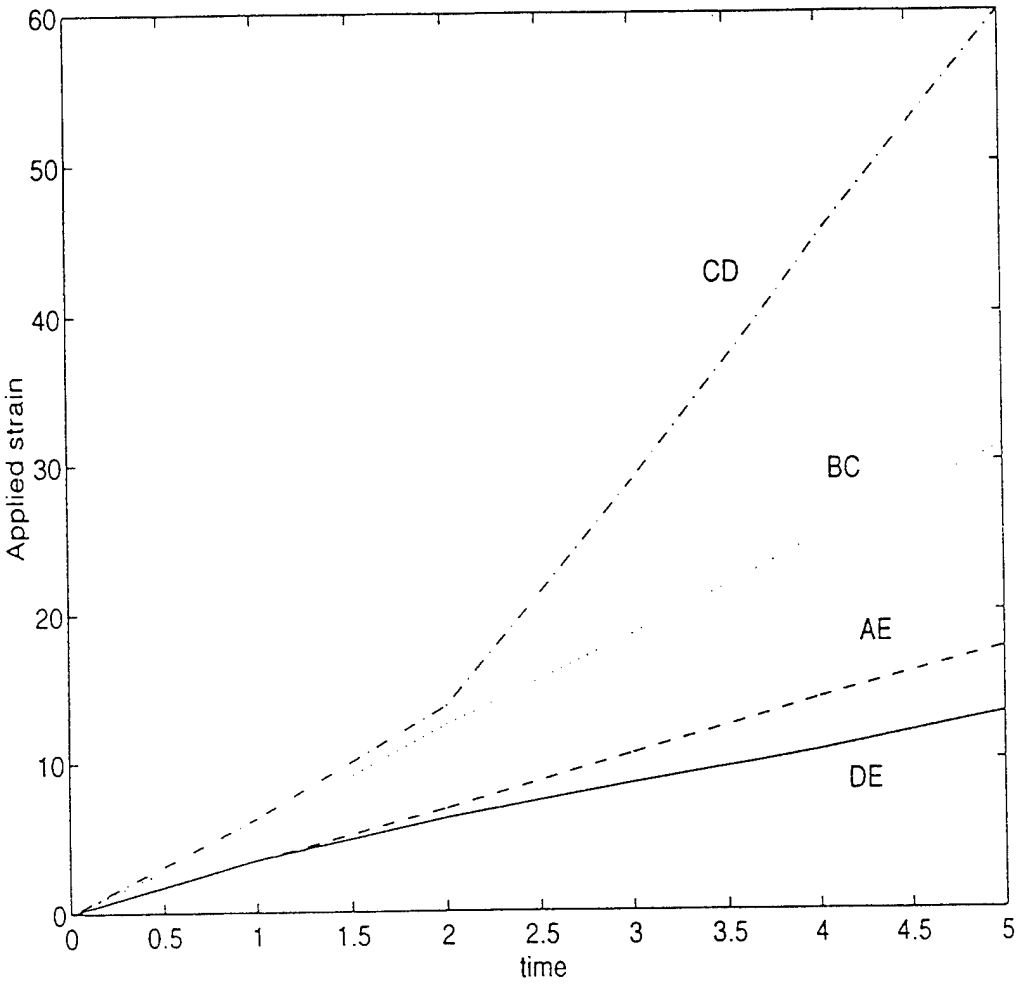

Figure 16. Local Stress-Strain Curves of a Tensile Specimen in Figure 15

stress-strain curve remains the same, there can exist many, different variations of particle distribution all having the same overall stress-strain curve. In the modeling, two different variations of 65 percent particle volume fraction (PVF) were used. The subdivisions of the model consisted of two regions divided along the line parallel to the horizontal axis whose areas are approximately the same. Specifically, the first variation consisted of .55 particle volume fraction in the lower half (the half where the hole resides) with .75 particle volume fraction in the upper half. In the second variation, the .75 particle volume fraction was placed in the lower half. The overall particle volume fraction for both of these variations were .65 PVF. The overall stress-strain curve for each PVF was estimated using a micromechanical model and the graphs are shown in Figures 17 and 18. The crack growth as a function of applied load for a perforated specimen was compared between the two cases. This is shown in Figure 19. In the figure, "low" denotes the lower half of the domain including the hole while "high" denotes the upper half of the domain, the half where the load is applied. The results indicated that the crack behavior around the notch tip strongly depended on the material property around the notch, more specifically, the particle distribution. Moreover, the graph shows that for the case where the lower half is .75 PVF, the strain (load) reaches up to the maximum value of .2 in/in, and the crack has advanced as far as it will go at a crack size/hole radius value of .75. The lower graph, the one with .55 PVF in the lower half, shows that the crack has propagated further along than the upper graph under much less load. For the purpose of looking at the initial crack propagation,

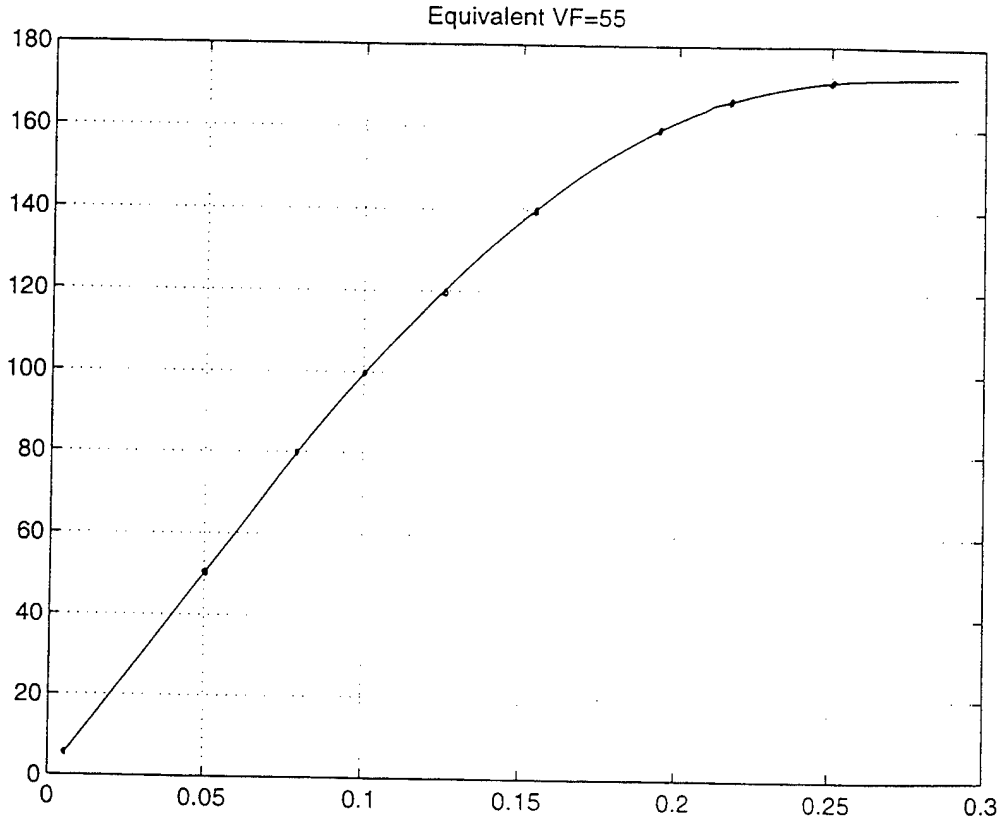

Figure 17. Stress-Strain Curve for Homogenous Material with Equivalent V.F. of .55

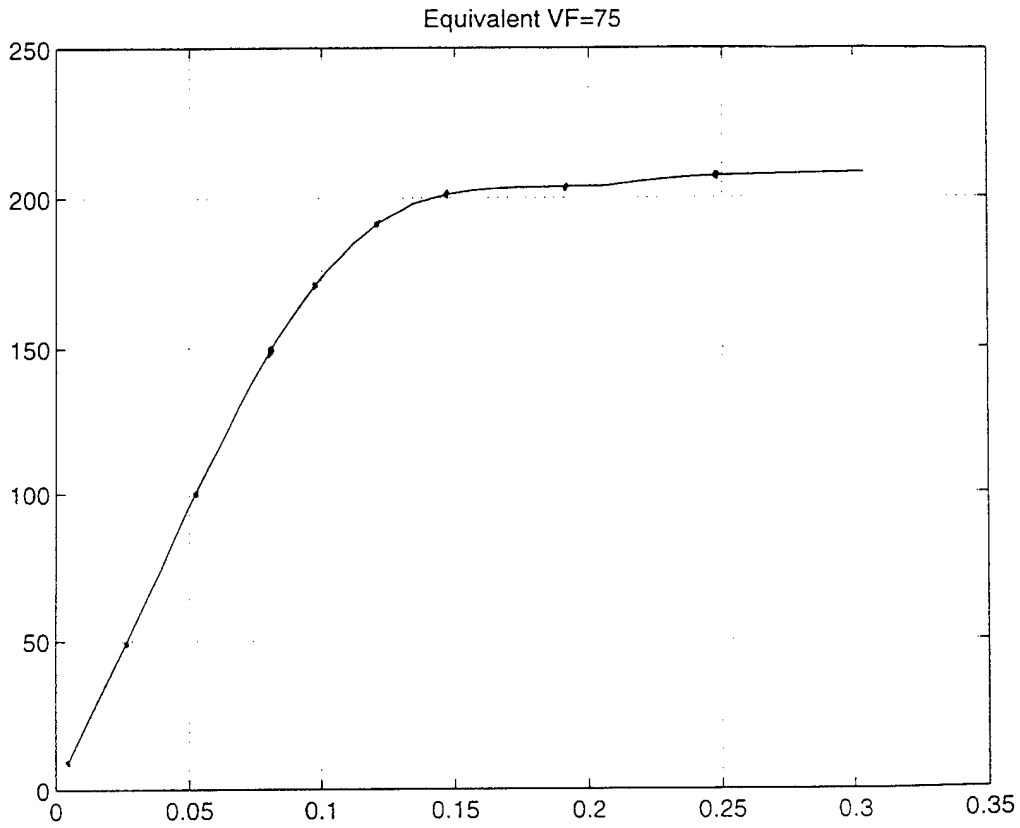

Figure 18. Stress-Strain Curve for a Homogenous Material with Equivalent V.F. of .75

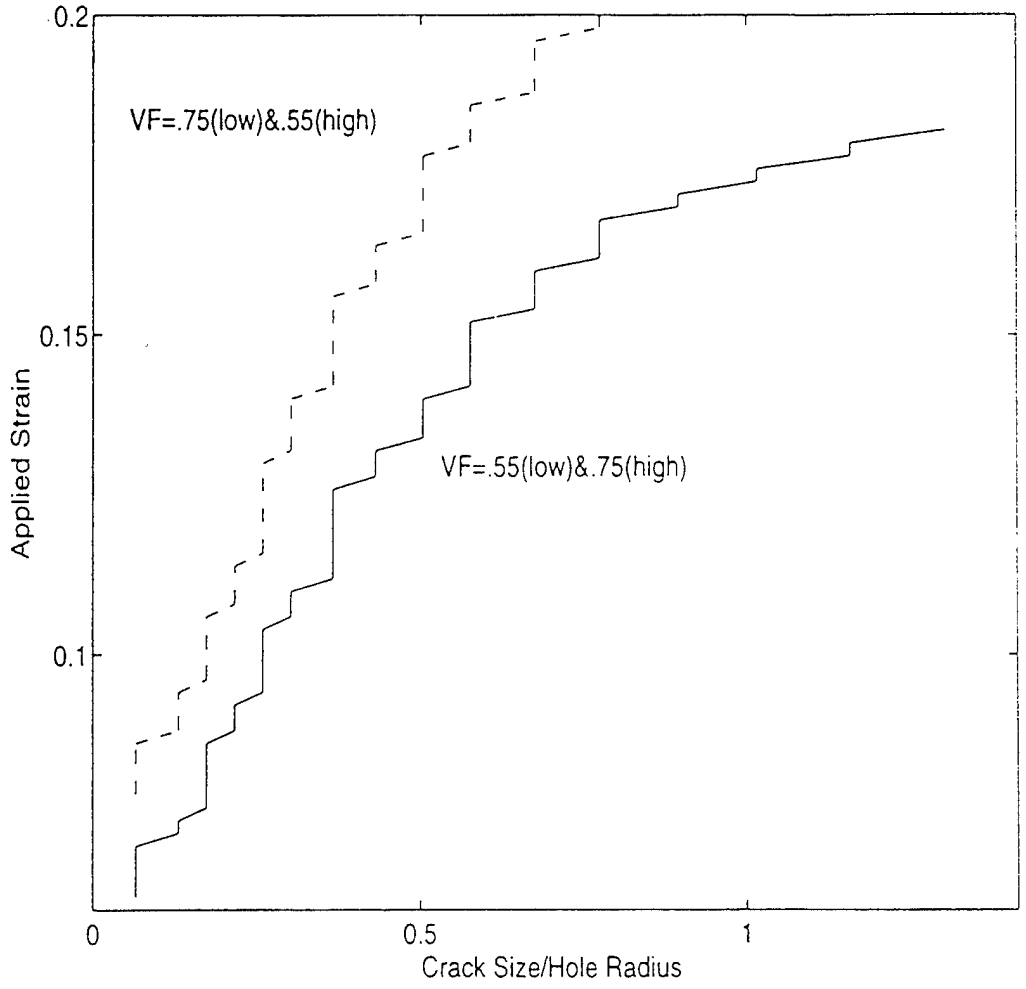

Figure 19. Crack Behavior in Nonuniform Materials

the graph was terminated at around the point where the crack reached 14 elements along the bottom edge of the model. If we were to look at the whole model, however, the second graph extends all the way across indicating complete failure in the model before reaching the maximum load of .2 in/in strain. In Figure 20, the crack propagation for the two volume fractions .55 and .75 are graphed. Instead of having mixed volume fractions, these are the cases when the entire model was homogeneously at .55 PVF and .75 PVF. As can be seen, the two curves terminate before reaching the maximum load of .2 in/in strain. If the curves are extended, just as in the mixed case where .55 PVF was in the lower half, the model undergoes a complete failure. Why is it then that when the volume fraction is homogenous at .55 PVF or .75 PVF the model fails completely but when they are mixed together, (specifically, .75 PVF in the lower half and .55 PVF in the upper half) crack only propagates to a point significantly before the complete failure? This is because two competing factors are at work. In the case of .55 PVF, the material is relatively soft, so it experiences less stress for the same deformation, but the strength of the material is low as well. Therefore, the load overcomes the strength and failure occurs. Similarly, in the case of .75 PVF, since the material is stiffer, for the same amount of load the stress experienced is much higher. However, the strength of the material is higher as well but not enough to overcome the load, and so, the failure occurs. When the volume fractions are mixed in the combination of .75 PVF in the lower half and .55 PVF in the upper half, the stress it experiences is greater than that of the homogenous case with volume fraction of .55 but lower than that of .75 PVF which

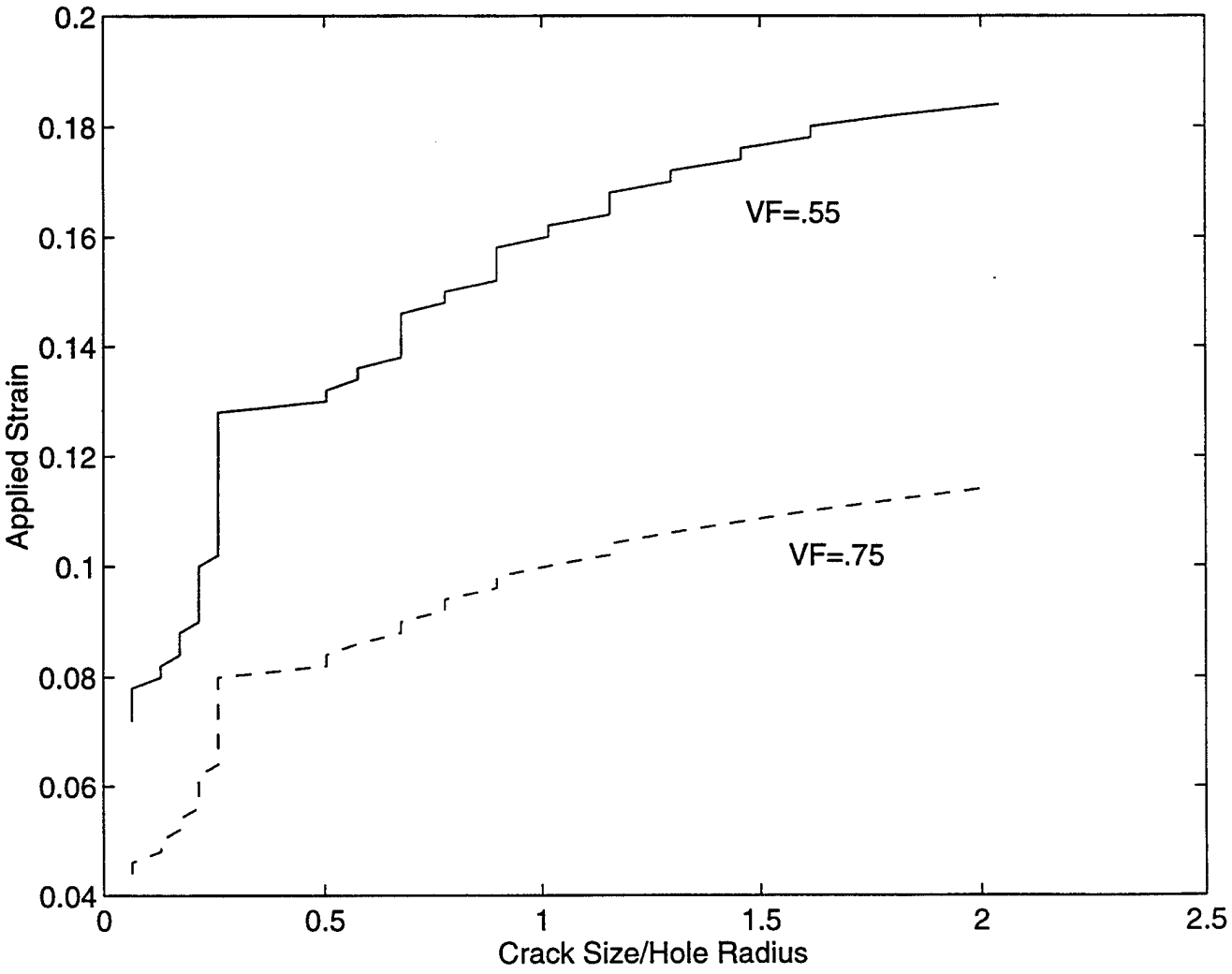

Figure 20. Plot of Crack Propagation for V.F. = .55 & .75

is as expected. But this time, the stress has decreased enough so that the strengthening effect of the .75 PVF overcomes the load. This results in the crack propagation being arrested before reaching complete failure.

The next study investigated the interaction of a notch tip and a pre-existing local defect such as a local cluster of particles or an inclusion of a void. Therefore, a local zone ahead of the notch tip was assumed to have a much higher stiffness or a much lower stiffness that the composite material depending on the type of inclusion. They are represented by the shaped regions in the figure. Specifically, this was modeled with the stiffness being greater or lesser by a factor of 10^6. These effects were examined on the initiation and growth of a crack from the notch tip. Figure 21 shows the locations of the inclusion. Specifically, they were placed at .183 cm (.072 in.), .411 cm (.162 in.), and .953 cm (.375 in.) from the edge of the hole. Figure 22 is a plot of the crack growth with a void at two different locations. When the void was located at the distance of 2.75 times the hole radius (i.e. void at .345 in.), the void did not affect the crack initiation and growth at the early stage because of the distance being too far from the place of crack initiation. However, as the crack propagated toward the void and became closer, the void affected the crack growth more significantly. On the other hand, when the void was placed at a distance much closer to the hole edge, at a distance of .183 cm (.072 in.), the crack initiation developed at a much smaller load (i.e. applied strain), and the crack propagated at a load lower than that of the case where there was no void. The study indicated that for the present particulate composite

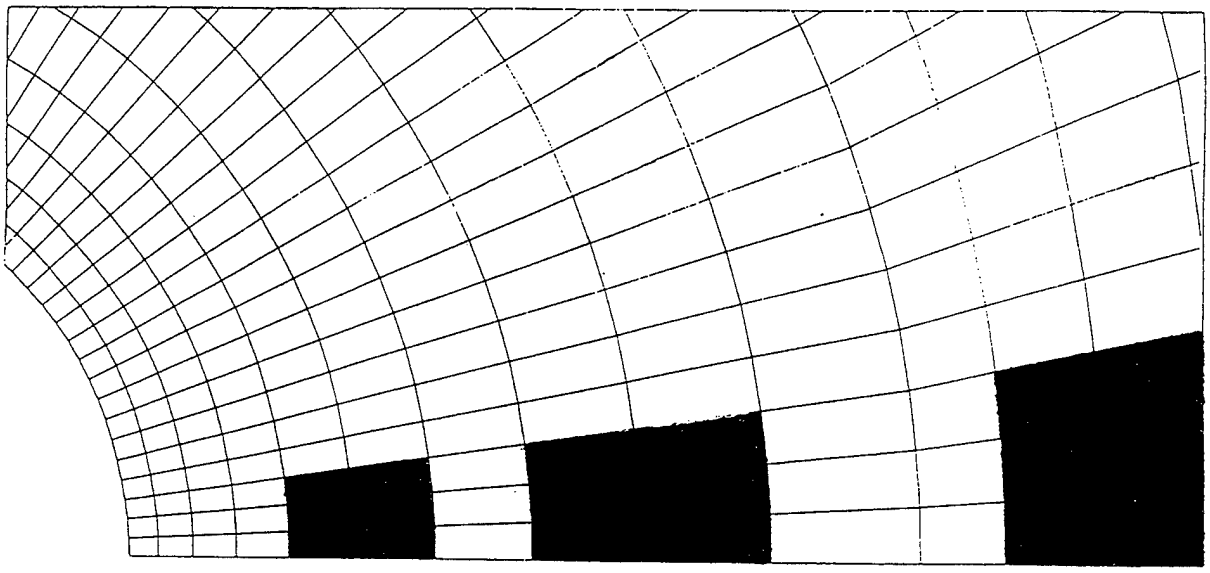

Figure 21. Locations of Void or Particle Cluster Inclusions

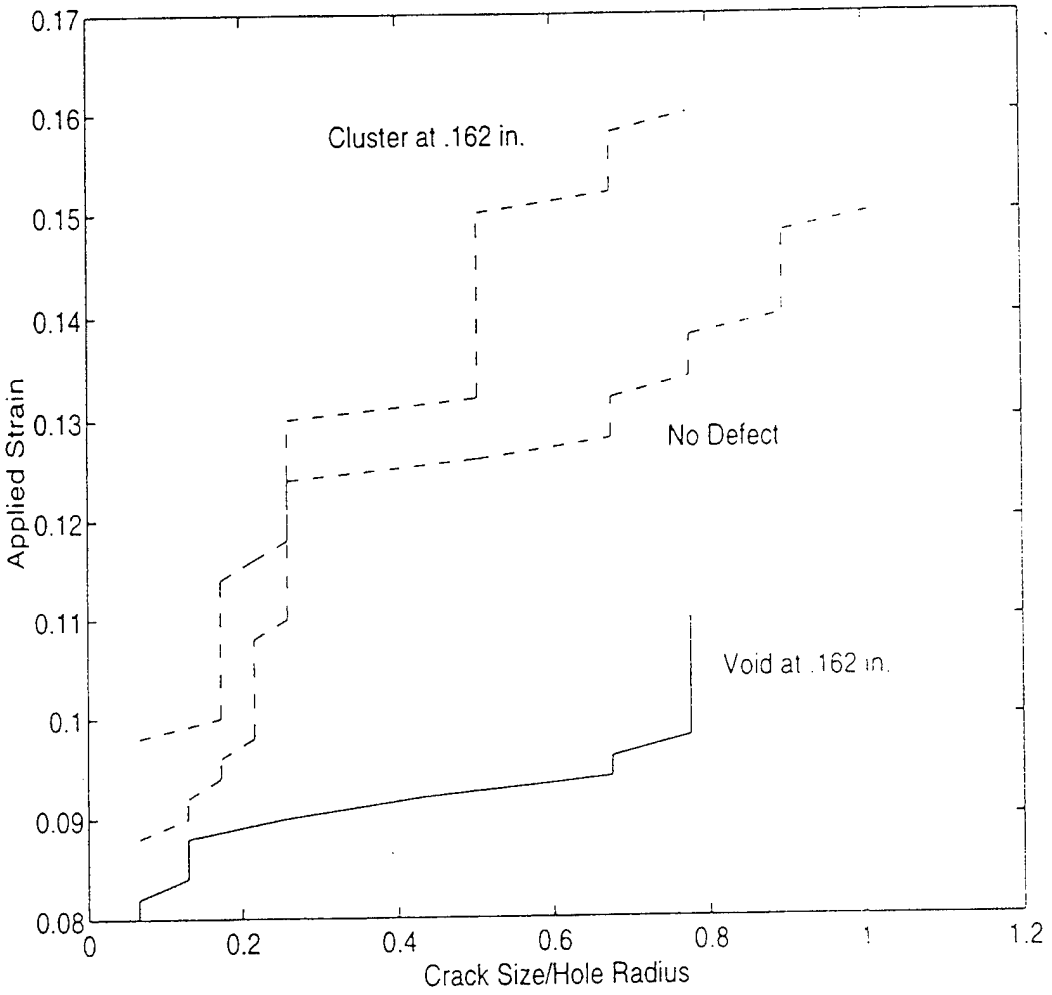

Figure 22. Effects of a Particle Cluster Near Circular Notch

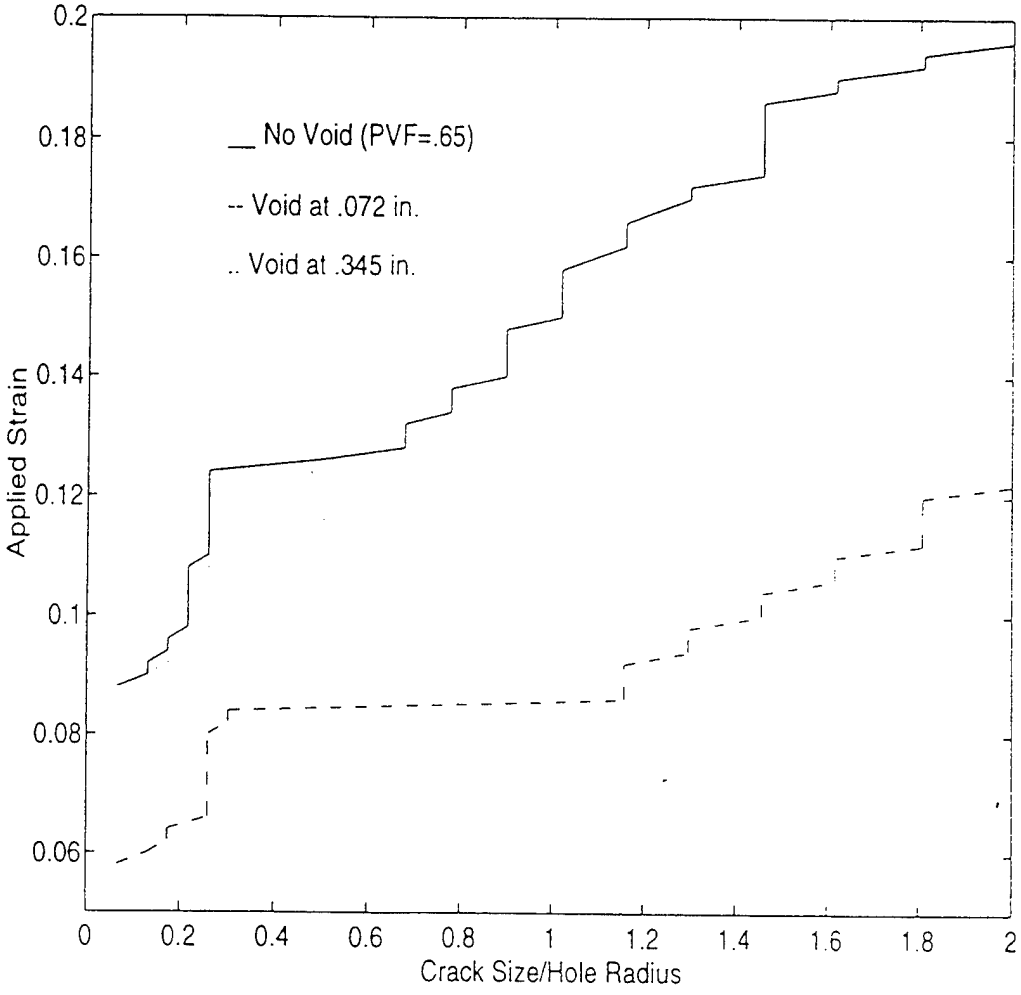

Figure 23. Effects of a Local Void Near a Circular Notch

material, an inclusion of a void at a distance about the size of the hole diameter from the edge made almost no difference in the initial crack. Figure 23 compares the crack growth between the cases with a void and a particle cluster, respectively, at the same distance from the hole edge. As expected, a particle cluster prevented the crack initiation and its growth compared to the no inclusion case. On the other hand, the presence of a void assisted in the crack initiation and growth.

The final study compared the damage and crack between two cases for a model with a hole diameter of 1.27 cm (.5 in.). The first case involved applying the load with a uniform traction which will be called traction control, and the second case involved applying the load with a uniform displacement load which will be called displacement control. The two cases, although different in form, had the same amount of total applied load. Figure 24 shows the comparison of the boundary edge traction between the traction control and the displacement control cases. The displacement control begins with a stress value lower than that of the traction control case but then increases as the distance along the x-axis increases. The traction control in the mean while stays constant. In Figure 25, the comparison of boundary edge displacement is shown. Here, the displacement for the traction control begins above the displacement control then decreases to a final value under the constant displacement control curve. These two figures collectively show that the traction control resulted in a larger load at the hole location, and also, the boundary edge displacement was greater as well. As a result, the

traction control yielded a greater damage zone and a longer crack size in the vicinity of the hole.

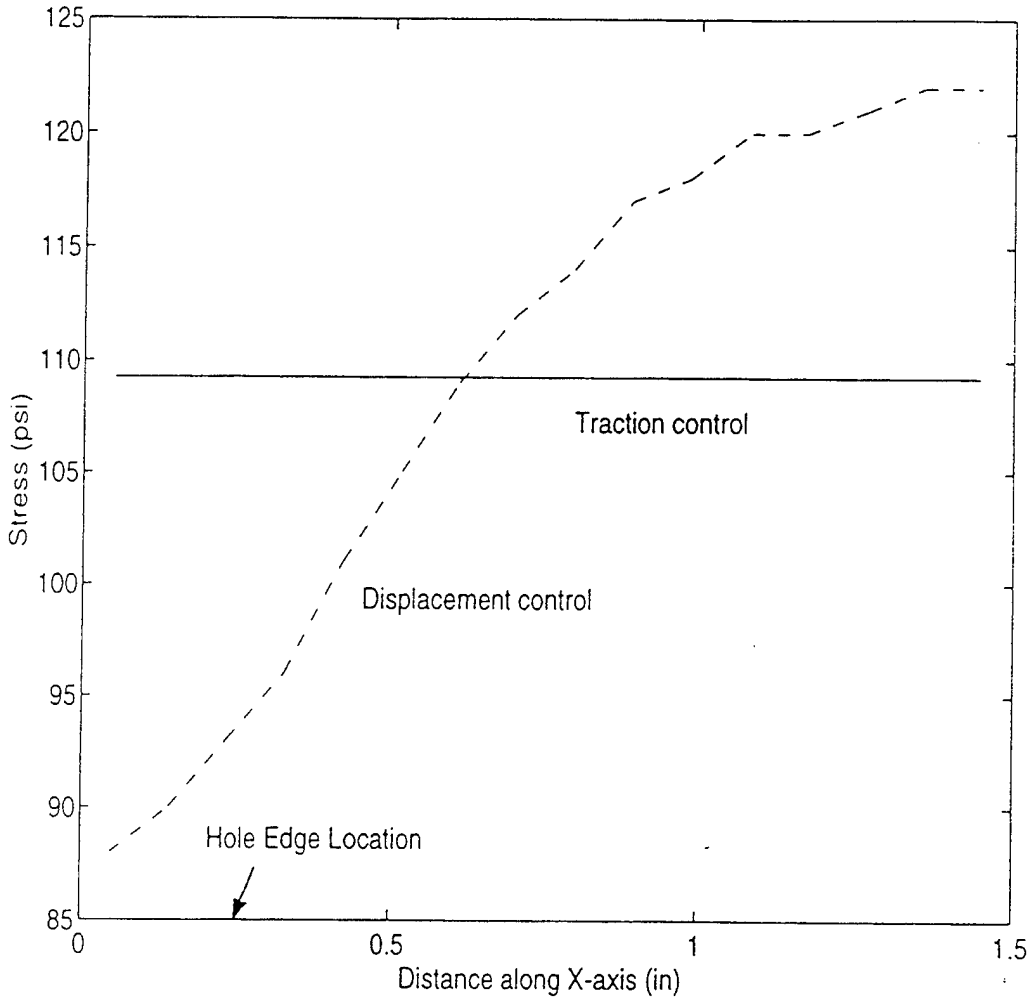

Figure 24. Comparison of Boundary Edge Traction for a Perforated Plate Between the Traction Control and the Displacement Control

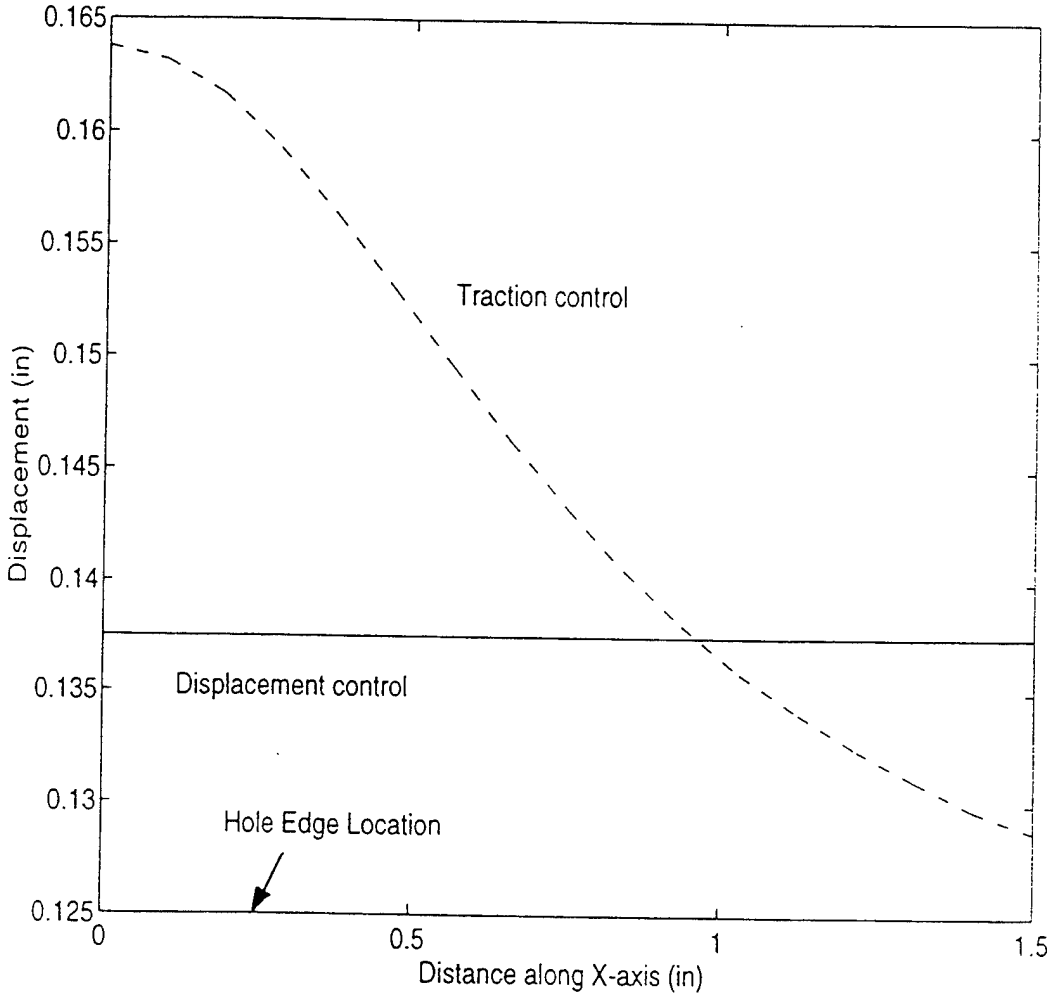

Figure 25. Comparison of Boundary Edge Displacement for a Performated Plate Between the Traction Control and the Displacement Control

VII. MICRO/MACROMECHANICS RESULTS AND DISCUSSION

The analysis used in this approach simulated the matrix damage initiation and damage propagation using the micromechanical model and the damage mechanics as described in Chapter IV. When the damage was saturated in a local zone, the location could not sustain any additional loading. Therefore, it was assumed that a crack occurred within the saturated damage zone. In other words, the crack length was deemed to be equal to the size of the saturated damage zone. Again, the stress-strain curve for the material used in the study is provided in Figure 26. This curve represents the macro-level, smeared material property. The micromechanical model requires the material properties of the constituent materials and their volume fractions. However, initially, this information is not known. Therefore, it is necessary to back calculate the micro-level material properties from the macro-level material properties using the proposed micromechanical model and the damage mechanics. The computed micro-level material properties were as follows:

- particle elastic modulus (10 x 10^6 psi)
- matrix elastic modulus (335 psi)
- volume fraction (.65)

In addition, the damage initiation strength of the matrix material calculated using equation (37) in Chapter IV was 70 psi, with damage material constants being a_1=92 psi and a_2=12 psi. The reproduced stress-strain curve using the micromechanical model and the damage mechanics is

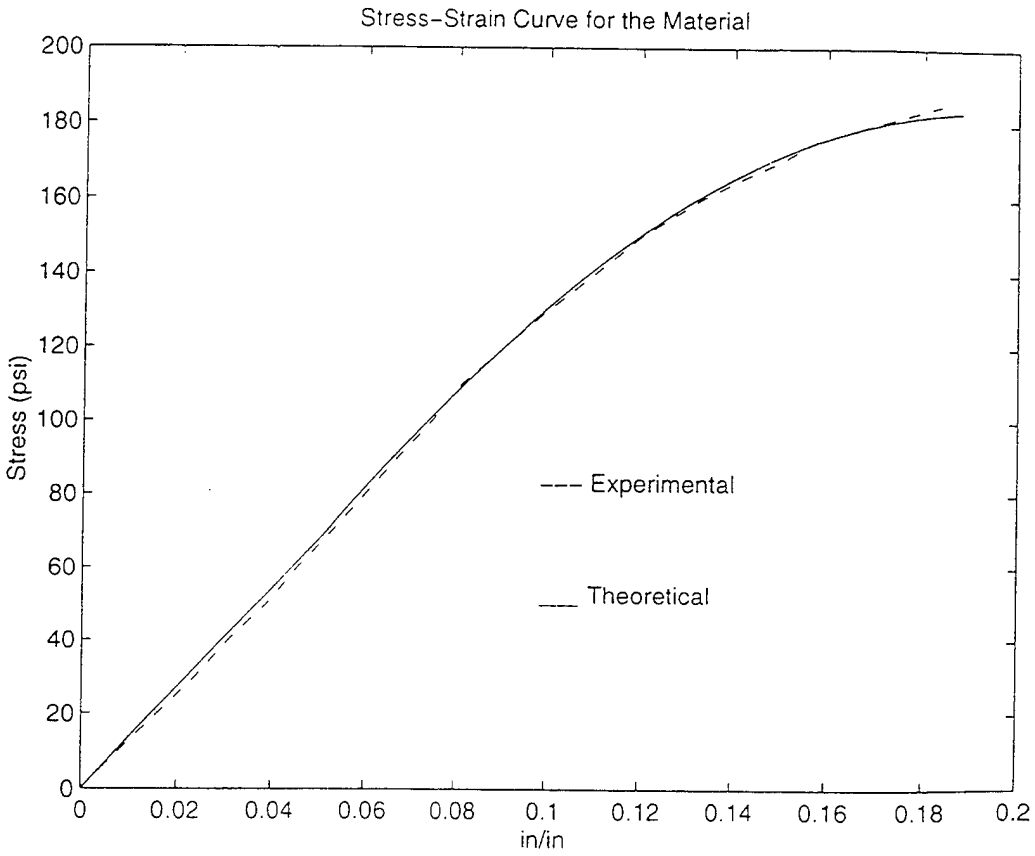

Figure 26. Comparison of Stress-Strain Curves Between the Experimental and the Theoretical

superimposed on the experimental stress-strain curve in Figure 26. As can be seen, the experimental curve and the predicted curve corresponded well to one another. By this comparison, the micro-level material values were deemed to be reasonably accurate.

The composite material was now tested with a hole in the center. Tensile loads were applied to the specimens with constant crosshead speed of .2 in/min. Cracks initiated from stress concentration at the edges of the holes. Figures 27 through 29 show the cracks in the specimens at strain of .2 in/in. Two of the specimens had .25 in. diameter holes while the third specimen had a .50 in. diameter hole. The first two specimens with the same diameter hole show two very different crack lengths under the same load as shown in Figures 27 and 28. In the third specimen (the one with .50 in. diameter hole), the crack lengths on the two sides of the hole came out to be quite asymmetric, as shown in Figure 29. These test results can be explained from the nonhomogeneity of particle distribution in the matrix material. As observed from the tensile test of a dogbone shaped specimen (without a hole), the local strain was very different from location to location within the specimen under the same, constant load. (Refer to Figure 16) The experimental stress-strain curve in Figure 26 is an average strain between the gauge length of 2.7 in. Therefore, when a hole is drilled into a specimen, the hole may be drilled into a particle-dense zone or into a particle-sparse zone without affecting the overall stress-strain curve. Because the specimen was under strain control, the local strain and stress around the hole varied depending on what type of topography (particle-dense

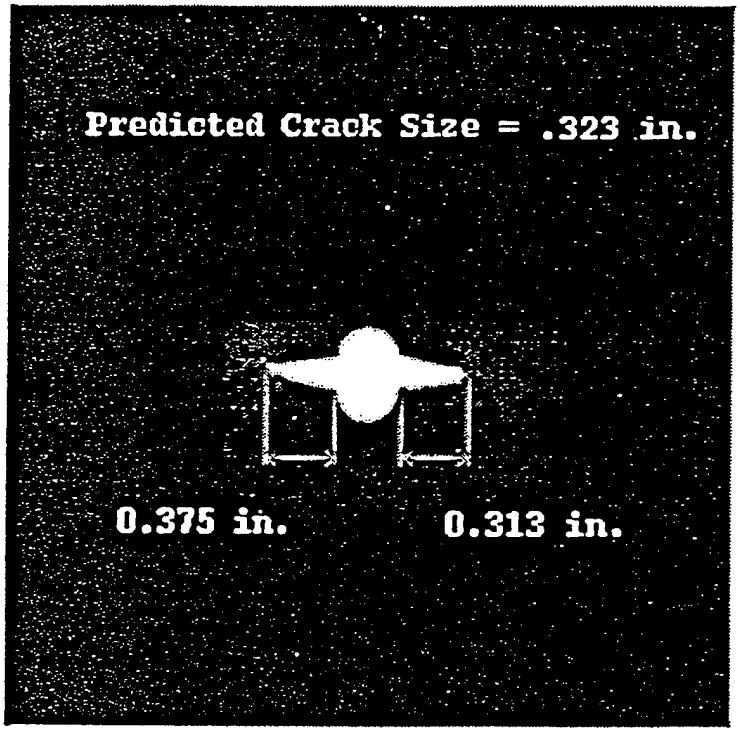

Figure 27. Comparison of Experimental and Theoretical Crack Sizes for a 0.25 in. Diameter Hole Sample

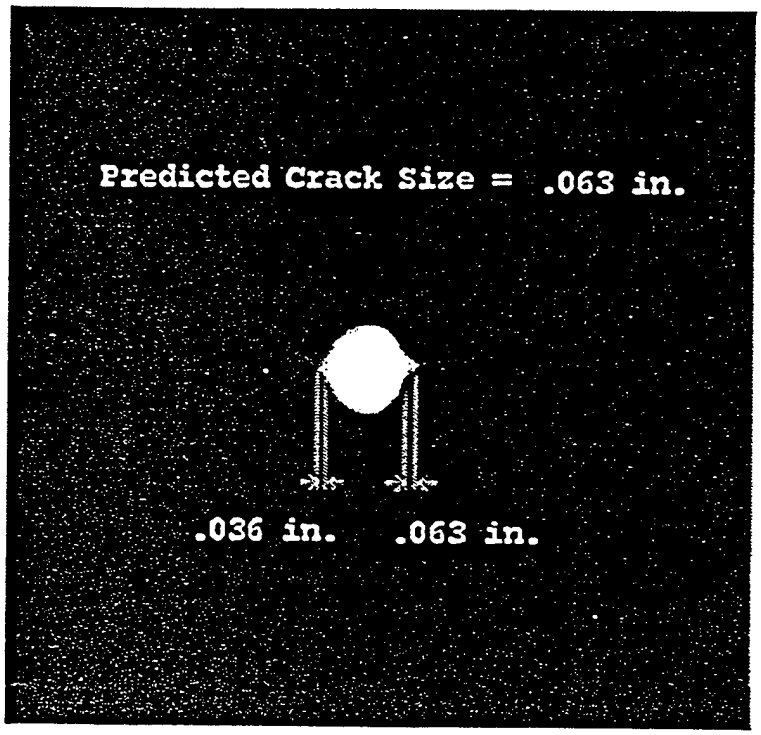

Figure 28. Comparison of the Experimental and Theoretical Crack Sizes for Another 0.25 in Diameter Hole Sample

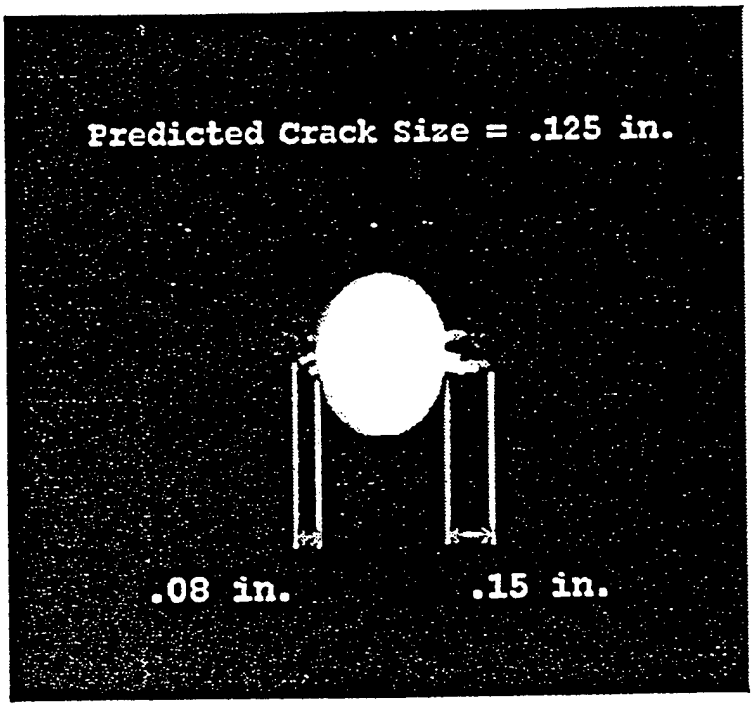

Figure 29. Comparison of Experimental and Theoretical Crack Sizes for a 0.5 in. Diameter Hole Sample

or particle-sparse) the hole was placed. Therefore, it was quite possible to have two different crack sizes for the same material, under similar conditions which was the case in our experiment. Similarly, the asymmetric cracks observed in the third specimen can be explained by the same reasoning as well as other factors such as asymmetric hole shape, location, and misaligned loading.

Computer simulation was conducted next to examine if similar results can be obtained and thereby, test the accuracy of the micro/macromechanics method in predicting the crack initiation and propagation. Initially, it was assumed that the specimen had a uniform material property (i.e. uniform particle distribution). The specimen with a .25 in. diameter hole was considered first. A quarter of the specimen was modeled as illustrated in Figure 3. The predicted crack size obtained from the computer simulation is shown in Figure 27 along with the actual cracks obtained from the experiment. The predicted crack length came out to be .340 in. while the experimental crack lengths were .375 in. and .313 in. The predicted crack length corresponded well to the experimental values for this sample.

In the simulation for the second specimen, a mixture of particle volume fractions was used. Figure 30 shows the division of the model. Two cases were considered. The first case considered the lower half of the specimen at a PVF of .55 and the upper half at a PVF of .75. In the second case, the particle volume fractions were switched so that the lower half had a PVF of .75 while the upper half had a .55 PVF. However, in both cases, the average PVF of .65 was maintained. The particle volume fraction (PVF)

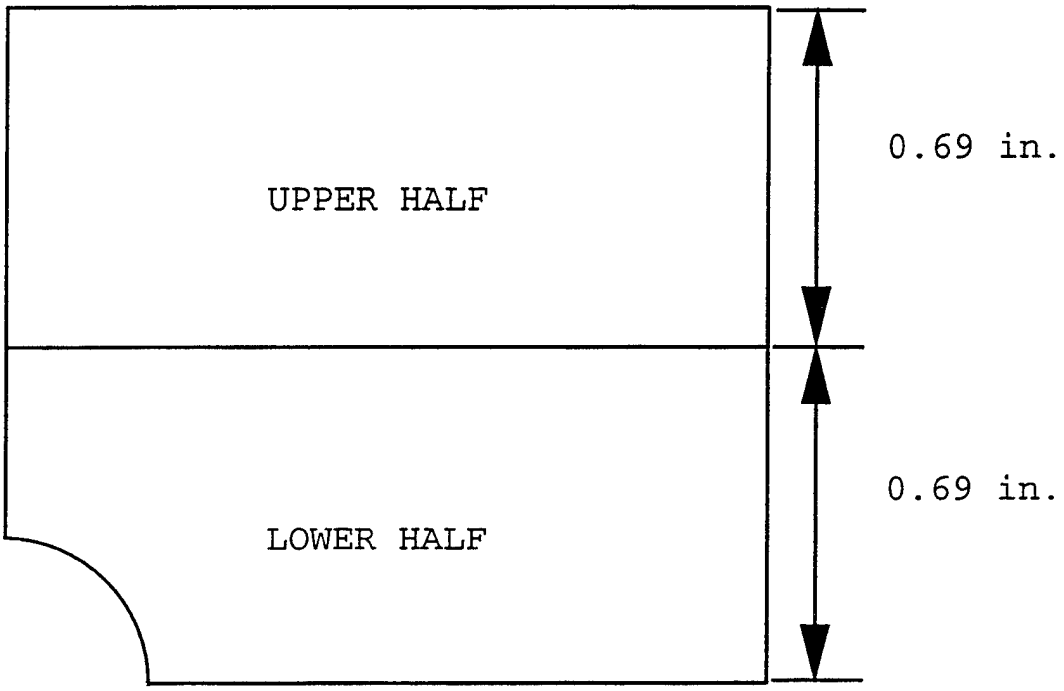

Figure 30. Shows the Division of the Model Between the Upper Half and the Lower Half

represent the degree of particle inclusion in the matrix material such that greater the PVF, greater the amount of particle inclusion. So, in the first case where the hole lied in the particle-sparse zone, the predicted crack size came out to be .063 in. which exactly matched one of the experimental crack lengths. The other experimental crack length was .036 in. On the other hand, the second case yielded a predicted crack length of .460 in. which was significantly higher than either of the experimental values. This indicates that the cracks produced in the experiment was due to the hole being drilled into a particle-sparse zone.

Some other related studies were undertaken next to investigate the crack initiation and propagation under different conditions. This time, different particle volume fractions were considered. The particle distribution was assumed to be uniform across the specimen with a .25 in. diameter hole at various PVF's. These models were then placed under the same loading conditions as before, and the results were obtained. The crack size verses applied strain is plotted in Figure 31. As expected, the graphs shows that the higher the PVF, the larger the crack size under the sample applied strain. One thing to be noted here is that when the PVF was .7 or higher, the crack size increased continuously without a halt as the specimen was stretched. On the other hand, when the PVF was .65 or lower, there was a temporary halt in the crack propagation as the specimen was stretched. Specifically, the crack did not propagate at certain lengths until there was a significant jump in the applied load. This phenomena was interpreted to indicate a crack blunting process. Also, when the PVF was .55, a large

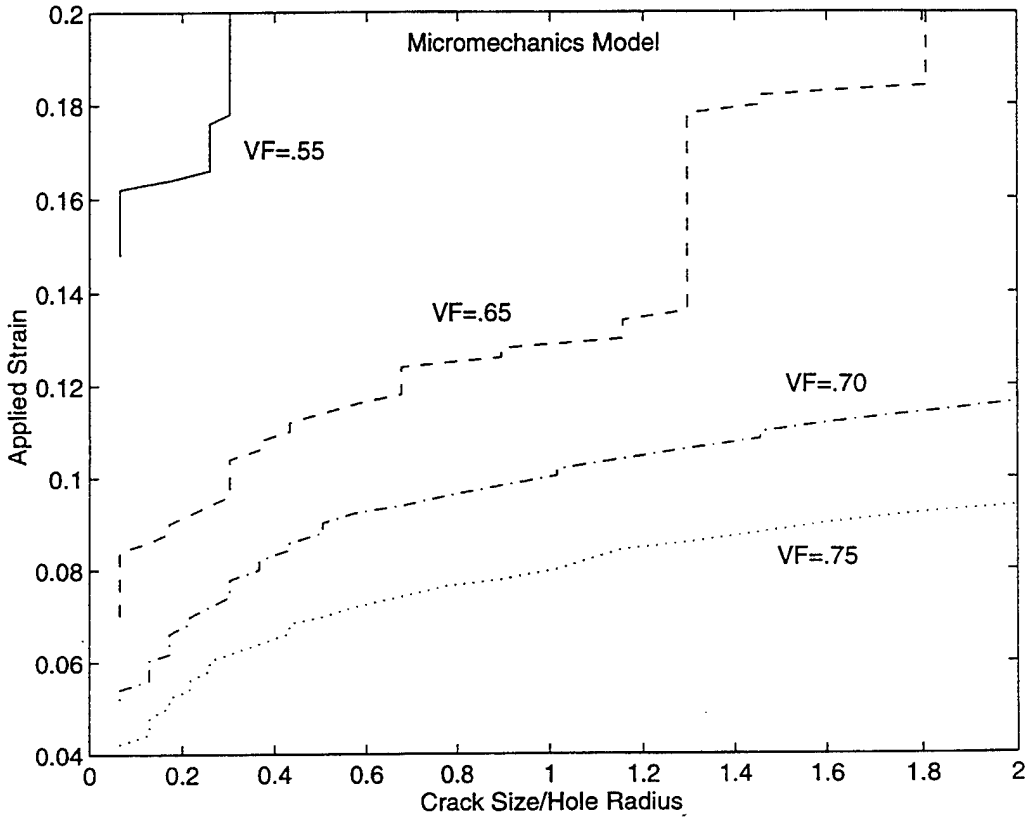

Figure 31. Crack Propagation of Various Volume Fractions Under Displacement Loading

increase in the applied strain was needed to initiate a crack.

The next study conducted was the response due to stress control. Uniform traction was applied at the top edge of the specimen and was increased continuously. The crack growth with different PVF's is given in Figure 32. The results indicated that the crack size increased continuously at almost the same rate as the applied load regardless of PVF. Under this type of loading, the stress state was similar that there was not much difference in the crack size among the various PVF's. A higher PVF yielded a lower stress in the matrix, because the particles supported a larger portion of the load. Hence, the higher PVF, the smaller the crack size. But again, the difference was hardly noticeable and was much less than that of the displacement control models. This outcome was as predicted. Since the load was in the form of a uniform stress, the stress experienced throughout the material was uniform although the deformation changed from point to point.

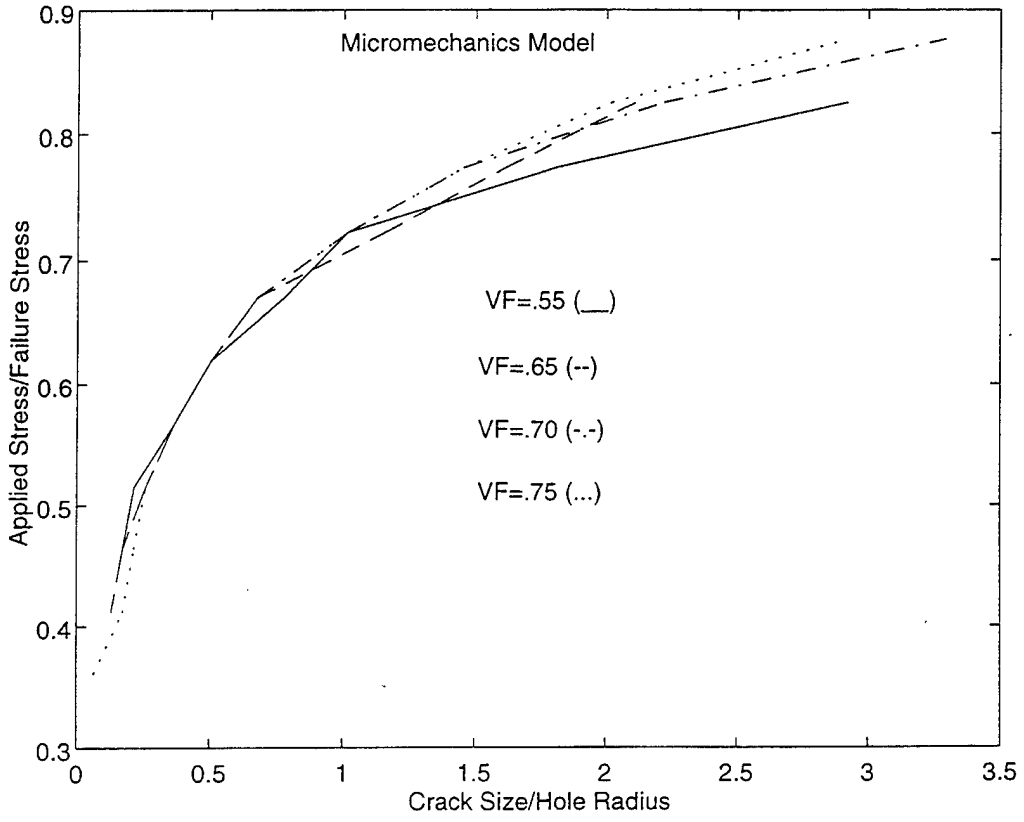

Figure 32. Crack Propagation of Various Volume Fractions Under Traction Loading

VIII. CONCLUSIONS AND RECOMMENDATIONS

Modeling of crack initiation and propagation in a particulate composite (solid rocket propellant) material was conducted using macromechanical and micro/macromechanical theories. The macromechanical studies showed that the crack behavior obtained from the experiment could be reproduced using finite element methods and a smeared, homogenous material property representing the particulate composite. Also, the interpretation of damage growth and saturation observed in the model as being the initiation and propagation of a crack was accurate. In the micro/macromechanical model and the damage mechanics, it was shown that the micro/macromechanical approach in predicting matrix cracking in particulate composites was appropriate and accurate. Furthermore, this approach was able to easily model the nonuniformity in particle distribution in the composite material. The predication of the crack size in a nonuniformly distributed composite was in good correspondence with the experimental results. Further analysis indicated that the displacement control of tensile specimens resulted in a smaller crack size for a smaller PVF subjected to the same global strain. On the other hand, the load controlled specimens yielded quite the opposite results. However, the displacement controlled specimens produced a much larger difference among the different PVF's than the load controlled specimens.

Recommendations for further study are as follows: Incorporate time depnedent effects such as strain rate effect and viscous effects, include more complex load conditions such as biaxial and shear loading, and conduct

analysis on an actual, operational propellant material. The composite used in this study was an inert material with a similar composite, material structure.

APPENDIX

SAMPLE INPUT FOR TRACTION LOAD (MICROMECHANICS)

```
806  1  17 2 0 2 10 0 0
0.0 19.  1.  1.  1.0e-4  1.0e-4  1.0
0  0  0  0  0  0
0  0  0  0
0  750 0 0
0 0
0 0
1 6
1.  10000000.  335.  0.2  0.5 2000.   70. 5000. 7000. 0.65
1.  1.   90.0   12.0 0.  0.  0.  0.  0.  0.
0.  0.  0.  0.  0.  0.  0.  0.  0.  0.
0.  0.  0.  0.  0.  0.  0.  0.  0.  0.
1     5     0    0.125000E+00   -0.426851E-17    0.000000E+00
2     5     0    0.134329E+00    0.000000E+00    0.000000E+00
3     5     0    0.145435E+00    0.000000E+00    0.000000E+00
4     5     0    0.159176E+00    0.000000E+00    0.000000E+00
*     *     *      *             *               *
*     *     *      *             *               *
*     *     *      *             *               *
803     6     0   -0.905402E-17    0.104009E+01    0.000000E+00
804     6     0   -0.627097E-17    0.114304E+01    0.000000E+00
805     6     0   -0.325488E-17    0.125460E+01    0.000000E+00
806     6     0   -0.213426E-15    0.137500E+01    0.000000E+00
 1     1   806   780   779   805
 2     1   805   779   778   804
 3     1   804   778   777   803
 4     1   803   777   776   802
 5     1   802   776   775   801
 *     *     *     *     *     *
 *     *     *     *     *     *
 *     *     *     *     *     *
746     1   760   786   787   761
747     1   761   787   788   762
748     1   762   788   789   763
749     1   763   789   790   764
750     1   764   790   791   765
390 2
0. 0.
20. 9.375
416 2
0. 0
20. 18.75
442 2
0. 0.
20. 18.75
468 2
0. 0.
* *
* *
* *
20. 18.75
780 2
0. 0
20. 18.75
806 2
0. 0.
20. 9.375
```

SAMPLE INPUT FOR DISPLACEMENT LOAD WITH MULITPLE MATERIAL

```
806  2  17 2 0 1 10 0 0
0.0 10. 1. 1. 1.0e-3 1.0e-3 1.0
0  0  0  0  0  0
0  0  0  0
0  750 0 0
0  0
0  0
1 4
1700.  7. 0.5 1.0 0. 0. 0. 1003.54 1026.59 928.38
803.25 683.72 515.17 311.65 108.37 6. 0. 0. 0. 0.
0. 0. 0. 0. 0. 0. 0. 0. 0. 0.
0. 0. 0. 0. 0. 0. 0. 0. 0. 0.
2 4
1700.  7. 0.5 1.0 0. 0. 0. 1893.04 1941.36 1765.
1321.98 802.28 324.42 51.63 57.32 6. 0. 0. 0. 0.
0. 0. 0. 0. 0. 0. 0. 0. 0. 0.
0. 0. 0. 0. 0. 0. 0. 0. 0. 0.
1    5    0   0.250000E+00   -0.426851E-17    0.000000E+00
2    5    0   0.262500E+00    0.000000E+00    0.000000E+00
3    5    0   0.275000E+00    0.000000E+00    0.000000E+00
4    5    0   0.287500E+00    0.000000E+00    0.000000E+00
5    5    0   0.300000E+00    0.000000E+00    0.000000E+00
6    5    0   0.312500E+00    0.000000E+00    0.000000E+00
7    5    0   0.325000E+00    0.000000E+00    0.000000E+00
*    *    *       *               *               *
*    *    *       *               *               *
*    *    *       *               *               *
803    6    0    0.157596E-16    0.104009E+01    0.000000E+00
804    6    0    0.109154E-16    0.114304E+01    0.000000E+00
805    6    0    0.566550E-17    0.125460E+01    0.000000E+00
806    6    0   -0.213426E-15    0.137500E+01    0.000000E+00
 1    1  806  780  779  805
 2    1  805  779  778  804
 3    1  804  778  777  803
 4    1  803  777  776  802
 5    1  802  776  775  801
 6    1  801  775  774  800
 *    *    *    *    *    *
 *    *    *    *    *    *
 *    *    *    *    *    *
748    1  762  788  789  763
749    1  763  789  790  764
750    1  764  790  791  765
390 2
0. 0.
10. 2.948
416 2
0. 0.
10. 5.896
0. 0.
* *
* *
* *
780 2
0. 0
10. 5.896
806 2
0. 0.
10. 2.948
```

SAMPLE INPUT FOR DISPLACEMENT LOAD (MICROMECHANICS)

```
806  1  0 0 0 0 1 0 17
0.0  100.  1.  1.  1.0e-4  1.0e-4  1.0
0  0  0  0  0  0
0  0  0  0
0  750  0  0
0  0
0  0
1  6
1.  10000000.  335.  0.2  0.5 2000.  70. 5000. 7000. 0.65
1.  1.  90.0  12.0 0.  0.  0.  0.  0.  0.
0.  0.  0.  0.  0.  0.  0.  0.  0.  0.
0.  0.  0.  0.  0.  0.  0.  0.  0.  0.
1     5     0    0.250000E+00   -0.426851E-17    0.000000E+00
2     5     0    0.262500E+00    0.000000E+00    0.000000E+00
3     5     0    0.275000E+00    0.000000E+00    0.000000E+00
4     5     0    0.287500E+00    0.000000E+00    0.000000E+00
5     5     0    0.300000E+00    0.000000E+00    0.000000E+00
6     5     0    0.312500E+00    0.000000E+00    0.000000E+00
7     5     0    0.325000E+00    0.000000E+00    0.000000E+00
*     *     *       *              *              *
*     *     *       *              *              *
*     *     *       *              *              *
801     6     0    0.242738E-16    0.859152E+00    0.000000E+00
802     6     0    0.202087E-16    0.945540E+00    0.000000E+00
803     6     0    0.157596E-16    0.104009E+01    0.000000E+00
804     6     0    0.109154E-16    0.114304E+01    0.000000E+00
805     6     0    0.566550E-17    0.125460E+01    0.000000E+00
806     7     0   -0.213426E-15    0.137500E+01    0.000000E+00
 1    1   806   780   779   805
 2    1   805   779   778   804
 3    1   804   778   777   803
 1    1   803   777   776   802
 5    1   802   776   775   801
 6    1   801   775   774   800
 *    *    *     *     *     *
 *    *    *     *     *     *
 *    *    *     *     *     *
747     1   761   787   788   762
748     1   762   788   789   763
749     1   763   789   790   764
750     1   764   790   791   765
390 2 .25
416 2 .25
442 2 .25
* * *
* * *
* * *
754 2 .25
780 2 .25
806 2 .25
```

SAMPLE INPUT FOR DISPLACEMENT LOAD (MACROMECHANICS CASE)

```
806  2  0 0 0 2 1 0 17
0.0  100.  1.  1.  1.0e-3  1.0e-3  1.0
0  0  0  0  0  0
0  0  0  0
0  750  0  0
0  0
0  0
1  4
1700.  13.  0.5  1.0  0.  0.  0.  1294.  110.  1142.9
130.  930.2  150.  689.7  170.  512.8  180.  220.2  192.  6.
0.  0.  0.  0.  0.  0.  0.  0.  0.  0.
0.  0.  0.  0.  0.  0.  0.  0.  0.  0.
2  1
1000.  12940000.  0.5  1.0  0.  0.  0.  0.  0.  0.
0.  0.  0.  0.  0.  0.  0.  0.  0.  0.
0.  0.  0.  0.  0.  0.  0.  0.  0.  0.
0.  0.  0.  0.  0.  0.  0.  0.  0.  0.
1    5    0    0.125000E+00   -0.426851E-17    0.000000E+00
2    5    0    0.134329E+00    0.000000E+00    0.000000E+00
3    5    0    0.145435E+00    0.000000E+00    0.000000E+00
4    5    0    0.159176E+00    0.000000E+00    0.000000E+00
5    5    0    0.176205E+00    0.000000E+00    0.000000E+00
6    5    0    0.197077E+00    0.000000E+00    0.000000E+00
*    *    *      *             *               *
*    *    *      *             *               *
*    *    *      *             *               *
803    6    0   -0.905402E-17    0.104009E+01    0.000000E+00
804    6    0   -0.627097E-17    0.114304E+01    0.000000E+00
805    6    0   -0.325488E-17    0.125460E+01    0.000000E+00
806    7    0   -0.213426E-15    0.137500E+01    0.000000E+00
 1    1   806  780  779  805
 2    1   805  779  778  804
 3    1   804  778  777  803
 1    1   803  777  776  802
 5    1   802  776  775  801
 6    1   801  775  774  800
 7    1   800  774  773  799
 *    *   *    *    *    *
 *    *   *    *    *    *
 *    *   *    *    *    *
748    1   762  788  789  763
749    1   763  789  790  764
750    1   764  790  791  765
390 2 .2751
416 2 .2751
442 2 .2751
 * * *
 * * *
 * * *
754 2 .2751
780 2 .2751
806 2 .2751
```

SAMPLE INPUT FOR TRACTION LOAD (MACROMECHANICS CASE)

```
806  1  17 2 0 2 10 0 0
0.0 10. 1. 1. 1.0e-4 1.0e-4 1.0
0  0  0  0  0  0
0  0  0  0
0  750 0 0
0 0
0 0
1 6
1. 10000000. 335. 0.2 0.5 2000.  70. 5000. 7000. 0.65
1. 1.  90.0  12.0 0. 0. 0. 0. 0. 0.
0. 0. 0. 0. 0. 0. 0. 0. 0. 0.
0. 0. 0. 0. 0. 0. 0. 0. 0. 0.
1    5    0   0.125000E+00   -0.426851E-17   0.000000E+00
2    5    0   0.134329E+00    0.000000E+00   0.000000E+00
3    5    0   0.145435E+00    0.000000E+00   0.000000E+00
4    5    0   0.159176E+00    0.000000E+00   0.000000E+00
5    5    0   0.176205E+00    0.000000E+00   0.000000E+00
6    5    0   0.197077E+00    0.000000E+00   0.000000E+00
7    5    0   0.222285E+00    0.000000E+00   0.000000E+00
8    5    0   0.252279E+00    0.000000E+00   0.000000E+00
9    5    0   0.287474E+00    0.000000E+00   0.000000E+00
*    *    *      *             *              *
*    *    *      *             *              *
*    *    *      *             *              *
*    *    *      *             *              *
798    6    0  -0.196987E-16    0.646339E+00   0.000000E+00
799    6    0  -0.179823E-16    0.709830E+00   0.000000E+00
800    6    0  -0.160672E-16    0.780671E+00   0.000000E+00
801    6    0  -0.139455E-16    0.859152E+00   0.000000E+00
802    6    0  -0.116101E-16    0.945540E+00   0.000000E+00
803    6    0  -0.905402E-17    0.104009E+01   0.000000E+00
804    6    0  -0.627097E-17    0.114304E+01   0.000000E+00
805    6    0  -0.325488E-17    0.125460E+01   0.000000E+00
806    6    0  -0.213426E-15    0.137500E+01   0.000000E+00
 1    1  806  780  779  805
 2    1  805  779  778  804
 3    1  804  778  777  803
 4    1  803  777  776  802
 5    1  802  776  775  801
 6    1  801  775  774  800
 7    1  800  774  773  799
 *    *    *    *    *    *
 *    *    *    *    *    *
 *    *    *    *    *    *
 *    *    *    *    *    *
746    1  760  786  787  761
747    1  761  787  788  762
748    1  762  788  789  763
749    1  763  789  790  764
750    1  764  790  791  765
390 2
0. 0.
10. 3.9315
416 2
0. 0
10. 7.863
*  *
*  *
*  *
780 2
0. 0
10. 7.863
806 2
0. 0.
10. 3.9315
```

LIST OF REFERENCES

1. Christensen, R. M., "A Critical Evaluation For A Class of Micromechanics Models", *J. Mech. Phys. Solids,* Vol. 38, 1990, pp. 379-404.

2. Hashin, Z., "The Elastic Moduli of Heterogenous Materials", *J. of Applied Mechanics,* 1962, pp. 143-150.

3. Lloyd, D. J., "Aspects of Fracture in Particulate Reinforced Metal Matrix Composites", *Acta metall. mater.,* Vol. 39, 1991, pp. 59-71.

4. Shen, Y. L., Finot, M., Needleman, A., and Suresh, S., "Effective Elastic Response of Two-Phase Composites", *Acta metall. mater.,* Vol. 42, 1994, pp. 77-97.

5. Jones, R. M., *Mechanics of Composite Materials,* Scripta Book Co., Washington D.C., 1975.

6. Farris, R. J. and Shapery, R. A., "Development of a Solid Rocket Propellant Nonlinear Viscoelastic Constitutive Theory", Technical Report AFRPL-TR-73-50, Air Force Rocket Propulsion Laboratory, Edwards, CA.

7. Schapery, R. A., "Analysis of Damage Growth in Particulate Composite Using a Work Potentila", *Compos. Engng,* Vol. 1, 1991, pp. 167-182.

8. Ravichandran, G and Liu, C. T., "Modeling Constitutive Behavior of Particulate Composites Undergoing Damage", *Int. J. of Solids Structures,* Vol. 32, No. 6/7, 1995, PP. 979-990.

9. Mochida, T., Taya, M., and Obata, M., "Effect of Damaged Particles on the Stiffness of a Particle/Metal Matrix Composite", *JSME Int. Jour. Series I,* Vol. 34, 1991, pp. 187-193.

10. Brechet, Y., Embury, J. D., Tao, S., and Luo, L., "Damage Initiation in Metal Matrix Composites", *Acta metall. mater.,* Vol. 39, 1991, pp. 1781-1786.

11. Kwon, Y. W. and Berner, J., "Analysis of Matrix Damage Evolution in Laminated Composite Plates", *Engineering Fracture Mechanics,* Vol. 48, 1994, pp. 811-817.

12. Kwon, Y. W. and Kim, C., "Progressive Damage Evaluation of Composite Structures Using Micro/Macromechanics and Damage Mechanics", *14th Army Symposium on Solid Mechanics,* October 1996, Myrtile Beach, South Carolina.

INITIAL DISTRIBUTION LIST

No. of Copies

1. Defense Technical Information Center 2
   8725 John J. Kingman Road, Ste 0944
   Ft. Belvoir, VA 22060-6218

2. Dudley Knox Library 2
   Naval Postgraduate School
   411 Dyer Rd.
   Monterey, CA 93943-5101

3. Professor Y. W. Kwon, Code Me/Kw 2
   Department of Mechanical Engineering
   Naval Postgraduate School
   Monterey, CA 93943-5002

4. Department Chairman, Code ME 1
   Department of Mechanical Engineering
   Naval Postgraduate School
   Monterey, CA 93943-5002

5. Naval Engineering Curricular Office (Code 34) 1
   Naval Postgraduate School
   Monterey, CA 93943-5002

6. Mr. James H. Lee 2

867 Cottonwood Dr.

Severna Park, MD 21146